

FABRICATION OF SILVER MICROBAND ELECTRODE ARRAYS
FOR ELECTROCHEMICAL DETECTION OF
HYDROGEN PEROXIDE



A Thesis Submitted in Partial Fulfillment of the Requirements for the
Degree of Master of Science in Chemistry
Suranaree University of Technology
Academic Year 2022

การประดิษฐ์อาร์เรย์ขั้วไฟฟ้าแถบไมโครเงินสำหรับการตรวจวัดไฮโดรเจน
เปอร์ออกไซด์ด้วยวิธีทางเคมีไฟฟ้า



วิทยานิพนธ์นี้เป็นส่วนหนึ่งของการศึกษาตามหลักสูตรปริญญาวิทยาศาสตรมหาบัณฑิต
สาขาวิชาเคมี
มหาวิทยาลัยเทคโนโลยีสุรนารี
ปีการศึกษา 2565

FABRICATION OF SILVER MICROBAND ELECTRODE ARRAYS FOR
ELECTROCHEMICAL DETECTION OF HYDROGEN PEROXIDE

Suranaree University of Technology has approved this thesis submitted in partial fulfillment of the requirements for a Master's degree.

Thesis Examining Committee



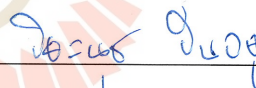
(Assoc. Prof. Dr. Sanchai Prayoonpokarach)
Chairperson



Asst. Prof. Dr. Kamonwad Ngamchuea
Member (Thesis Advisor)



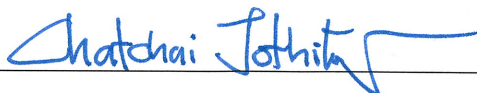
Asst. Prof. Dr. Patcharin Chaisuwan
Member



Dr. Piyanut Pinyou
Member



Dr. Pattanaphong Janphuang
Member



(Assoc. Prof. Dr. Chatchai Jothityangkoon)
Vice Rector for Academic Affairs
and Quality Assurance



(Prof. Dr. Santi Maensiri)
Dean of Institute of Science

กิริกิต แก้วเกตุ : การประดิษฐ์อาร์เรย์ขั้วไฟฟ้าแถบไมโครเงินสำหรับการตรวจวัดไฮโดรเจนเปอร์ออกไซด์ด้วยวิธีทางเคมีไฟฟ้า (FABRICATION OF SILVER MICROBAND ELECTRODE ARRAYS FOR ELECTROCHEMICAL DETECTION OF HYDROGEN PEROXIDE) อาจารย์ที่ปรึกษา : ผู้ช่วยศาสตราจารย์ ดร.กมลวัช งามเชื้อ, 56 หน้า

คำสำคัญ: ขั้วไฟฟ้าไมโครแบบอาร์เรย์, วิธีการลิโทกราฟีแบบใช้แสง, โวลแทมเมทรี, เซ็นเซอร์, เปอร์ออกไซด์

ในงานวิจัยนี้เป็นการประดิษฐ์ขั้วไฟฟ้าแถบไมโครเงินแบบอาร์เรย์สำหรับวิเคราะห์และตรวจวัดไฮโดรเจนเปอร์ออกไซด์ (H_2O_2) ที่สะดวกและรวดเร็ว โดยขั้วไฟฟ้าที่ผลิตขึ้นมานี้เป็นขั้วไฟฟ้าที่มีราคาถูก มีความทนทาน สามารถใช้ซ้ำได้ และใช้สารตัวอย่างในปริมาณน้อย ในขั้นตอนการตรวจวัดในตัวอย่างจริง เมื่อใช้ขั้วไฟฟ้าที่ผลิตขึ้นมานี้ไม่จำเป็นต้องมีขั้นตอนเตรียมตัวอย่าง ซึ่งช่วยลดการใช้ตัวทำละลายและลดเวลาในการวิเคราะห์ โดยก่อนนำขั้วไฟฟ้าไมโครเงินไปตรวจวัดไฮโดรเจนเปอร์ออกไซด์ต้องทำการกระตุ้นขั้วไฟฟ้าก่อนด้วยเทคนิคไซคลิกโวลแทมเมทรีโดยการออกซิไดซ์โลหะเงิน [$Ag_{(s)} \rightarrow Ag^+_{(aq)} + e^-$] และพอกพูนโลหะเงินอีกครั้ง [$Ag^+_{(aq)} + e^- \rightarrow Ag_{(s)}$] ในงานวิจัยนี้ได้ศึกษาผลกระทบของขนาดต่าง ๆ ของขั้วไฟฟ้าไมโครเงินต่อสัญญาณการตรวจวัดไฮโดรเจนเปอร์ออกไซด์ เช่น ความกว้าง ความยาว ระยะห่างระหว่างขั้วไฟฟ้า และความสูงของขั้วไฟฟ้ากับแถบเชื่อมต่อกับเครื่องมือ เมื่อใช้ขั้วไฟฟ้าที่พัฒนาขึ้นตรวจวัด H_2O_2 สามารถวัดซ้ำได้ดี (RSD = 1.12% (n=5)) และสามารถใช้ขั้วไฟฟ้าซ้ำได้ดี (RSD = 1.20% (n=5)) ขั้วไฟฟ้าที่พัฒนาขึ้นนี้มีสภาพไวสูงเท่ากับ $9.84 \pm 0.34 \mu A \text{ mM}^{-1}$ ช่วงความเป็นเส้นตรงอยู่ระหว่าง 0.0 – 10.0 mM และขีดจำกัดการตรวจวัดเท่ากับ 47.80 μM และได้มีการนำขั้วไฟฟ้าไมโครเงินนี้ตรวจวัด H_2O_2 ในตัวอย่างชนิดต่าง ๆ เช่น ตัวอย่างปัสสาวะสังเคราะห์ ตัวอย่างน้ำประปา ตัวอย่างน้ำดื่ม และตัวอย่างนม ด้วยวิธีการเติมสารมาตรฐานให้ค่าร้อยละการกลับคืนที่ใกล้เคียง 100% (RSD < 5%) ซึ่งสามารถตรวจวัดในตัวอย่างจริงได้อย่างถูกต้อง และแม่นยำ ซึ่งในขั้นตอนการตรวจวัดในตัวอย่างจริงในงานนี้เป็นการตรวจวัดสารโดยตรงที่ไม่ผ่านขั้นตอนการเตรียมตัวอย่างไม่จำเป็นต้องเจือจางตัวอย่างหรือเติมสารละลายอิเล็กโทรไลต์

สาขาวิชาเคมี

ปีการศึกษา 2565

ลายมือชื่อนักศึกษา กิริกิต แก้วเกตุ
ลายมือชื่ออาจารย์ที่ปรึกษา กมลวัช งามเชื้อ

KEERAKIT KAEWKET : FABRICATION OF SILVER MICROBAND ELECTRODE ARRAYS
FOR ELECTROCHEMICAL DETECTION OF HYDROGEN PEROXIDE. THESIS ADVISOR
: ASST. PROF. KAMONWAD NGAMCHUEA, Ph. D. 56 PP

Keywords: Microelectrode array, Photolithography, Voltammetry, Sensor, Peroxide

Silver microband electrode arrays (Ag-MEA) are fabricated by photolithography for a fast and simple one-step analysis of H₂O₂. The fabricated electrodes are low-cost, robust, reproducible, and require only a small volume of sample. No sample preparation is required, eliminating the use of solvent and reducing analysis time. Before the first usage of the electrode. The electrode activation, voltammetric oxidation [$\text{Ag}_{(s)} \rightarrow \text{Ag}^+_{(aq)} + e^-$] and re-deposition [$\text{Ag}^+_{(aq)} + e^- \rightarrow \text{Ag}_{(s)}$], is only required once before the first use. The effects of electrode sizes such as length, width, band-to-band separation, and the height of the connection strip towards the voltammetric responses of H₂O₂ are evaluated. The developed method shows excellent repeatability (RSD = 1.20% ($n = 5$)) and reproducibility (RSD = 1.12% ($n = 5$)) with the linear range of 0.0 – 10.0 mM, the sensitivity of $9.84 \pm 0.34 \mu\text{A mM}^{-1}$, and the limit of detection of 47.80 μM . The developed sensor has been successfully applied to detect H₂O₂ directly (without dilution of samples or addition of supporting electrolytes) in synthetic urine, tap water, drinking water, and milk samples with the % recoveries close to 100% (within $\pm 5\%$).

School of Chemistry
Academic year 2022

Student's signature กฤษฎิ์ แก้วบุญ
Advisor's signature กมล งามชูเอ

ACKNOWLEDGMENTS

I would like to express my special thanks of gratitude to all those who gave me the possibility to complete this work. First my thesis advisor, Asst. Prof. Dr. Kamonwad Ngamchuea. She gave me the golden opportunity to do this wonderful project on the topic “Fabrication of silver microband electrode arrays for electrochemical detection of hydrogen peroxide”, which also helped me in doing a lot of research. She taught me different ways to solve problems. She has provided valuable reviews, comments, and suggestions during the finalization of the document. I came to know about so many new things I am thankful to her. Secondly, Asst. Prof. Dr. Wittawat Saenrang and Dr. Pattanaphong Janphuang for teaching me and give me suggestion about the fabrication of microband electrode array using photolithography technique.

Finally, I would also like to thank my parents, friends and SUT electrochemical group laboratory who helped me a lot in finalizing this project within the limited time frame.



Keerakit Kaewket

CONTENTS

	Page
ABSTRACT IN THAI.....	I
ABSTRACT IN ENGLISH.....	II
ACKNOWLEDGMENTS.....	III
CONTENTS.....	IV
LIST OF FIGURES.....	VI
LIST OF TABLES.....	IIX
LIST OF ABBREVIATIONS.....	IX
CHAPTER	
I INTRODUCTION.....	1
1.1 Research and background.....	1
1.2 Research objectives.....	4
II LITERATURE REVIEW.....	5
2.1 Hydrogen peroxide.....	5
2.2 Current electrochemical methods for H ₂ O ₂ detection.....	6
2.3 Electrode fabrication: Photolithography.....	9
2.4 Electrode characterization.....	10
2.4.1 Cyclic voltammetry.....	10
2.4.2 Scanning electron microscope.....	11
III THEORY AND SIMULATION.....	13
3.1 Fundamentals of electrochemistry.....	13
3.1.1 Equilibrium electrochemistry.....	13
3.1.2 Dynamic electrochemistry.....	14
3.1.3 Mass transport in solution.....	15
3.2 Electrochemical cell.....	18

CONTENTS (Continued)

		Page
	3.3 Microelectrode	19
	3.4 Mathematic model and numerical simulation	21
	3.5 COMSOL Multiphysics	25
	3.6 Convergence study	26
IV	EXPERIMENTAL	28
	4.1 Chemical reagents	28
	4.2 Electrode fabrication and characterization	31
	4.3 Electrochemical measurements	32
	4.4 Application to real sample	322
V	RESULTS AND DISSCUSSION.....	34
	5.1 Simulation results	34
	5.2 Cyclic voltammetry of H ₂ O ₂ at Ag macroelectrode.....	36
	5.3 Characterization of Ag microband electrode arrays (Ag-MEA)	37
	5.4 Requirement of adhesion layer and electrode activation	39
	5.5 Effects of electrode size (<i>r</i>), separation distance (<i>d</i>), length (<i>l</i>), and height (<i>h</i>)	40
	5.6 Reproducibility tests.....	43
	5.7 Calibration curve.....	43
	5.8 Applications in synthetic urine, tap water, drinking water, and milk samples	44
VI	CONCLUSION.....	46
	REFERENCES	48
	CURRICULUM VITAE.....	56

LIST OF FIGURES

Figure	Page
2.1	Photolithography processes..... 9
2.2	Comparison of positive and negative photoresist. 10
2.3	a) A plot of the applied potential with time in CV. b) Cyclic voltammogram. 11
2.4	Principle of scanning electron microscope (SEM)..... 12
3.1	Schematic diagram of energy levels of a metal electrode and redox species A and B. 13
3.2	Schematic of typical mass transport..... 16
3.3	The model used in the explanation of Fick's law of diffusion..... 17
3.4	An electrochemical three-electrode cell set-up. 19
3.5	Diffusion regime of a) microelectrode and b) macroelectrode. 19
3.6	Schematic diagram of the four categories of a diffusion process at microelectrode arrays 21
3.7	a) cross section of the xz plane of the microband electrode. b) unit cell..... 22
3.8	a) Illustration of a microband electrode array (MEA) and the definitions of symbols: electrode size (r), electrode separation distance (d), electrode length (l), and height of the connection strip (h). b) Boundary conditions for the simulation of cyclic voltammetry at an MEA in a 2-dimensional unit cell. 24
3.9	An example of triangles mesh..... 26
4.1	Silver microband electrode array (Ag-MEA) fabrication by photolithography..... 32

LIST OF FIGURES (Continued)

Figure	Page	
5.1	<p>Simulated cyclic voltammograms at microband electrode array in 2D simulation space of a 1-electron process ($A + e^- \rightleftharpoons B$): a) Reversible, and b) Irreversible. Concentration profiles at $E - E_0 = 0$ V of A: c) Reversible, and d) Irreversible. $r = 20 \mu\text{m}$, $\nu = 50 \text{ mV s}^{-1}$, $\alpha = 0.5$, $T = 298 \text{ K}$, $D_A = D_B = 10^{-9} \text{ m}^2 \text{ s}^{-1}$, $c_A^* = 1 \text{ mol m}^{-3}$, $c_B^* = 0 \text{ mol m}^{-3}$. The images are in proportional scale.....</p>	35
5.2	<p>a) CV of 10.0 mM H_2O_2 in 0.10 M KCl at Ag macroelectrode (2.00 mm diameter) at the scan rate of 10 mV s^{-1}. The inlay shows the plot of $\ln I$ vs. E in Tafel analysis. b) CV of 10.0 mM H_2O_2 in 0.10 M KCl at varied scan rates. The inlay shows the plot of peak potentials (I_p) vs. square root of scan rates (ν).....</p>	37
5.3	<p>Microscopic images of Ag-MEA with $r = 20 \mu\text{m}$ (a-e) at different electrode separation distances: a) $d = 20 \mu\text{m}$, b) $d = 40 \mu\text{m}$, c) $d = 60 \mu\text{m}$, d) $d = 80 \mu\text{m}$, e) $d = 100 \mu\text{m}$. f) Photo of an Ag-MEA ($r = 20 \mu\text{m}$, $d = 20 \mu\text{m}$). Microscopic images of Ag-MEA with $r = 50 \mu\text{m}$ (g-k) at different electrode separation distances: g) $d = 50 \mu\text{m}$, h) $d = 100 \mu\text{m}$, i) $d = 150 \mu\text{m}$, j) $d = 200 \mu\text{m}$, k) $d = 250 \mu\text{m}$. l) Photo of an Ag-MEA ($r = 50 \mu\text{m}$, $d = 50 \mu\text{m}$) and m) SEM images of the Ag-MEA ($r = 20 \mu\text{m}$, $d = 20 \mu\text{m}$) at different magnification.</p>	38
5.4	<p>CV of 10.0 mM H_2O_2 in 0.10 M KCl at the scan rate of 50 mV s^{-1} at Ag MEA. a) Different adhesion layers: Ti (red) vs. Cr (black). b) Without activation (blue) vs. With activation (black). The inlay in b) shows the stripping and re-deposition of Ag in the activation of the electrode.....</p>	40

LIST OF FIGURES (Continued)

Figure	Page
5.5 CV of 10.0 mM H ₂ O ₂ in 0.10 M KCl at the scan rate of 50 mV s ⁻¹ at silver microband electrodes with a) different d: (black) 50 μm, (red) 100 μm, (blue) 150 μm; fixed r = 50 μm, l = 2.00 mm, h = 6.5 mm. b) different r: r = 20 μm, d = 20 μm vs. r = 50 μm, d = 50 μm vs. r = 20 μm, d = 100 μm vs. r = 50 μm, d = 100 μm. c) different l: (black) l = 2.00 mm vs. (pink) 5.00 mm (fixed r = 20 μm, d = 20 μm, h = 6.5 mm). d) different h: (black) h = 6.5 mm vs. (yellow) h = 11.7 mm.....	42
5.6 CV of varied concentrations of H ₂ O ₂ at the scan rate 50 mV s ⁻¹ . Ag-MEA in 0.10 M KCl.	44
5.7 Cyclic voltammograms of a) synthetic urine, b) tap water, c) drinking water, and d) milk spiked with different concentrations of H ₂ O ₂ in the recovery studies by standard addition method at an Ag-MEA electrode at the scan rate of 50 mV s ⁻¹	45

LIST OF TABLES

Table	Page
2.1 Previous research for the electrochemical method for H ₂ O ₂ detection.....	7
3.1 Parameter for boundary conditions.....	25
4.1 List of chemicals used in this work.....	28
4.2 List of chemicals used to prepare synthetic urine	30
4.3 Preparation of sample and standard solution.....	33
5.1 Measured sizes of the fabricated Ag-MEAs.....	39
5.2 Spike and recovery tests of H ₂ O ₂ in synthetic urine, tap water, drinking water, and milk samples.....	45

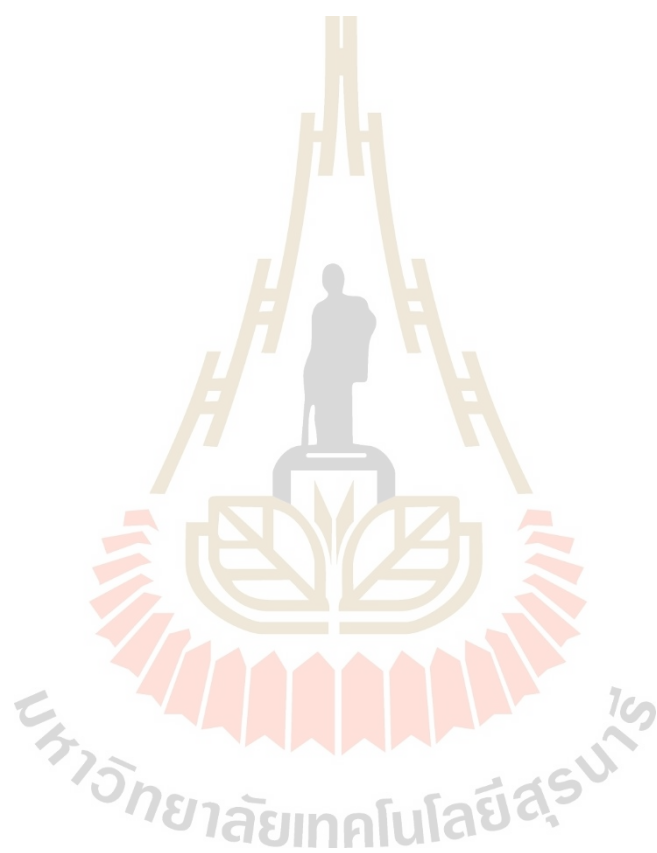


LIST OF ABBREVIATIONS

A	Electrode surface area
Ag-MEA	Silver microband electrode arrays
Amp	Chronoamperometry
c_0	Concentration at the electrode surface
CV	Cyclic voltammetry
D	Diffusion coefficient
d	Electrode separation distance
E	Potential
E_f^0	Formal potential
F	Faraday constant
FEA	Finite element analysis
GCE	Glassy carbon electrode
h	The height of the connection strip
l	The length of the electrode
I	Current
i	Current density
I_p	Peak current
i_p	Peak current density
J	Flux
k	The electrochemical rate constants
MOF	Metal organic framework
n	Number of electron transfer
PDEs	Partial differential equations
R	Gas rate constant
r	The electrode size
RSD	Relative standard deviation

LIST OF ABBREVIATIONS (Continued)

SEM	Scanning electrode microscope
SWV	Square wave voltammetry
<i>T</i>	Temperature
V	Voltage



CHAPTER I

INTRODUCTION

1.1 Research and background

Electrochemical measurements typically require the addition of supporting (electrochemically inert) electrolytes of up to 100 times in excess of the redox analyte at conventional macroelectrodes for diffusion to be the only mass transfer process in the system (Dickinson, Limon-Petersen, Rees, and Compton, 2009; Toh et al., 2013; Ward Jones, Campbell, Baron, Xiao, and Compton, 2008). Under insufficient electrolytic supports, the analysis of electrochemical response is complicated due to the contribution of migration. Significant distortion of voltammograms also occurs in the absence of supporting electrolyte due to Ohmic potential drop and the alteration in the electrical double layer, reducing the accuracy and sensitivity of the measurement.

In contrast to macroelectrodes, microscopic electrodes allow measurements in low ionic strength samples (Huang, O'Mahony, and Compton, 2009; K. Ngamchuea, C. Batchelor-McAuley, and R. G. Compton, 2018). Reduced Ohmic drop, high current density, high mass transfer flux, low background charging current, and possibilities of *in-vitro* and *in-vivo* applications are strong advantages of microelectrodes (K. Ngamchuea, C. Batchelor-McAuley, and R. G. Compton, 2018; K. Ngamchuea, C. Lin, C. Batchelor-McAuley, and R. G. Compton, 2017). However, low magnitude of currents at a microelectrode (typically pA – nA range) can be easily disturbed by electrical noises. A more advanced instrument is required to measure the low currents at microelectrodes. The signals at encapsulated microelectrodes can also be less effective than theoretically predicted due to stray capacitance (K. Ngamchuea, C. Lin, C. Batchelor-McAuley, and R. G. Compton, 2017).

These limitations can be overcome by the use of *microelectrode arrays* which enhance the current responses and sensitivities of the measurements while maintaining the beneficial characteristics of microelectrodes. Previous literatures have also reported the use of bipotentiostat or multipotentiostat with microelectrode arrays to enhance the current responses by redox cycling of the generated species at a collector electrode and improve the selectivity of the sensor by distinguishing between reversible and irreversible processes, for example, in the detection of dopamine (Chuang, Lai, Ho, and Chen, 2013), glucose (Han et al., 2020), and oxygen (Gondosiswanto, Hibbert, Fang, and Zhao, 2018).

Several techniques have been developed for the fabrication of microelectrode arrays including screen printing (Tan, Metters, and Banks, 2013), 3-D printing (Yang, Rahman, Du, Panat, and Lin, 2016), electrodeposition (Simm et al., 2005), nanoimprint lithography (Ugarte et al., 2015), and photolithography (Huang et al., 2009). A number of work has reported theoretical and experimental studies of microelectrode arrays of various geometries including microdisc (Menshykau et al., 2009), microband (Streeter et al., 2007), and interdigitated band electrodes (Barnes, Fernandez-la-Villa, Pozo-Ayuso, Castano-Alvarez, and Compton, 2015). Microelectrode arrays made of metals (Kannan, Hu, Morgan, Moshkalev, and Rout, 2016; Lee, Lim, Seo, Bishop, and Papautsky, 2007), metal oxides (D. Liu et al., 2021; X. Wang, Sun, Wang, and Shi, 2020), and carbon materials (Ng, Lim, Low, and Loh, 2015; Seddon, Shao, and Girault, 1994; Zhang, Liu, Zou, Zhang, and Xu, 2019) have been developed and employed in electrochemical detection of analytes such as heavy metals (Seddon et al., 1994), dissolved oxygen (Lee et al., 2007), pH (X. Wang et al., 2020), insecticides (W. Zhang et al., 2019), salicylic acid (D. Liu et al., 2021), dopamine (Ng et al., 2015), glucose (Frebel et al., 1997), L-lactate (Frebel et al., 1997), and uric acid (Frebel et al., 1997). The electrode material is chosen in accordance with the redox nature of the analyte, cost, robustness, intrinsic noise, and ease of fabrication.

In this work, silver microband electrode arrays (Ag-MEA) were fabricated by photolithography for direct detection of hydrogen peroxide (H_2O_2). H_2O_2 is a potentially toxic contaminant in water, foods, and the environment. The compound is widely used in fuel cells (Yamada, Yoneda, and Fukuzumi, 2013), energy storages (Jia, Wang, and

Wang, 2015; S. Liu, Pan, Li, and Gao, 2015; Martins et al., 2020; Wessells, Huggins, and Cui, 2011), bleaching reagents (Suliman, Addy, MacDonald, and Rees, 2004), disinfectants (Lubello, Caretti, and Gori, 2002), foods (Y. Li et al., 2020), and agricultural products (Nurnaeimah et al., 2020). Physiologically, H₂O₂ acts as a redox transmitter and is the product of several metabolic reactions (Winterbourn, 2013). An excess of H₂O₂ can cause damage to cells and tissues, leading to the development of diseases (Pravda, 2020; Winterbourn, 2013). The analysis of H₂O₂ is thus highly important in industry, environment, and biomedical applications. We therefore need to develop a H₂O₂ sensor which can function in various types of samples.

The overall reduction of H₂O₂ is a two-electron two-proton process, as follows:



At silver electrodes, the most commonly proposed mechanism of the electrochemical reduction of H₂O₂ in neutral condition is via the formation of OH_(ads) intermediate (Cai et al., 2018):



The electrochemical responses are strongly governed by the size of the microelectrode and the distance between adjacent electrodes relative to the diffusion layer thickness (Streeter et al., 2007). For microelectrode arrays, space should be used efficiently. However, the electrode separation also has to be sufficiently large such that there is no significant overlap of diffusional layers for the array to maintain the characteristics of microelectrodes, giving rise to efficient analytical performances (Chevallier et al., 2005; Trevor J. Davies, Banks, and Compton, 2005; Trevor J. Davies, Moore, Banks, and Compton, 2004). In order to develop the most efficient electrochemical sensors, it is important to also investigate the mass transport properties of the system along with the development of electrodes and detection methods. Herein, the effects of electrode adhesion layer, electrode activation process, electrode width, band-to-band separation, electrode length, and height of the connection strip towards the reduction of H₂O₂ were investigated in detail before application of the sensor in real samples.

1.2 Research objectives

This work aims to develop silver microelectrode arrays for electrochemical application. The objectives are as follows:

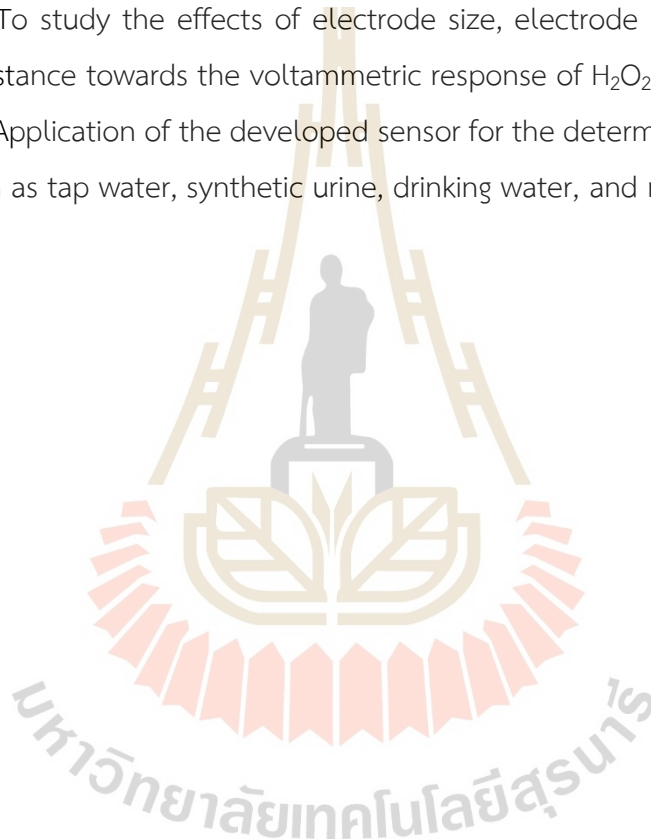
1.2.1 To develop an electrochemical sensor for the determination of H_2O_2 .

1.2.2 To fabricate the silver microelectrode array.

1.2.3 To study the mechanism and diffusion regime of H_2O_2 reduction and the electrochemical behaviour of H_2O_2 at microelectrode array.

1.2.4 To study the effects of electrode size, electrode length, and electrode separation distance towards the voltammetric response of H_2O_2 .

1.2.5 Application of the developed sensor for the determination of H_2O_2 in real samples such as tap water, synthetic urine, drinking water, and milk sample.



CHAPTER II

LITERATURE REVIEWS

2.1 Hydrogen peroxide

Hydrogen peroxide is a chemical which compound composed of two hydrogen atoms and two oxygen atoms, with a chemical formula of H_2O_2 . The redox reaction of hydrogen peroxide (H_2O_2) has an important role in many fields such as

- Fuel cells: H_2O_2 is used for catholyte i.e. It has a role for electrolyte and cathode (Yamada et al., 2013),
- Energy storages (Wessells et al., 2011, Liu et al., 2015),
- Bleaching reagents (Sulieman et al., 2004),
- Disinfectants (Lubello et al., 2002),
- Foods (Li et al., 2020),
- Agricultural products that used H_2O_2 for controlled pests such as aphids and red spider mites (Nurnaeimah et al., 2020),
- Dairy industry that used H_2O_2 for the preservation milk to destroy the enzyme lactoperoxidase. Lactoperoxidase has been proven to be effective against bacteria (Arefin, Sarker, Islam, Harun-ur-Rashid, and Islam, 2017).

In many countries, H_2O_2 is used for many fields such as the USA approved to use H_2O_2 for the preparation of whey, preservation of milk intended for cheese production, and dried egg products. In Canada, H_2O_2 is used in the production of beer and used for decolorizing and maintain pH in dried whey products (Uchida and Ono, 1999). According to US Environmental Protection Agency (EPA) recommendations, drinking water should have a residual H_2O_2 of 25 to 50 ppm (Watkins, 2009). The Australia New Zealand Food Standards Code allows to use H_2O_2 as processing aid in food industry. Food Standards Australia New Zealand set the maximum level of residual H_2O_2 in the final product to be 5.0 mg/kg.

When used incorrectly or in high concentration, hydrogen peroxide can be toxic and have a variety of negative effects on living organisms.

Toxicity to skin and eyes: The concentration of hydrogen peroxide can irritate and corrode the skin, eyes, and mucous membranes. Skin contact with hydrogen peroxide can result in skin redness, itching, burning, and even chemical burns. Direct contact of hydrogen peroxide with the eyes can cause severe eye irritation, redness, and tearing. In some cases, it can also damage the cornea and result in vision loss.

Toxicity of hydrogen peroxide with inhalation: When hydrogen peroxide enters the body through inhalation, its vapors can cause respiratory irritation, coughing, and difficulty breathing. Inhaling high concentrations of hydrogen peroxide can also cause lung damage leading to inflammation and swelling of the lung tissue.

Toxicity of hydrogen peroxide with ingestion: Ingesting hydrogen peroxide can result in irritation of the stomach, nausea, vomiting, and abdominal pain. Ingestion of high concentrations of hydrogen peroxide can result in more severe symptoms such as internal bleeding and metabolic acidosis.

The release of hydrogen peroxide into various water sources can decrease oxygen levels, which can have negative effects on aquatic animals. Additionally, hydrogen peroxide can react with other chemicals in the environment, producing harmful byproducts that can be detrimental to the environment.

In previous studies, hydrogen peroxide has been shown to be toxic to animals. The LD50 value in mice for intraperitoneal, intravenous, oral, skin, and subcutaneous exposure routes are 880, 50,000, 2,000, 12,000, and 1,072 mg/kg, respectively (Abdollahi and Hosseini, 2014).

2.2 Current electrochemical methods for H₂O₂ detection

Table 2.1 shows the previous research about the determination of H₂O₂ with the electrochemical method.

Table 2.1 Previous research for the electrochemical method for H₂O₂ detection.

Electrode	Method	Linear range	Limit of detection	Samples	Ref.
Platinum microelectrode array	Amp	1.0×10 ⁻⁶ to 1.0×10 ⁻⁵ M	not reported 6.743 pA/μM for sensitivity	Activated macrophages	(Carriere, Rodrigues, Tan, Arumugam, and Poh, 2021)
Ruthenium purple-modified carbon fiber microelectrodes	Amp	2.0×10 ⁻⁶ to 5.0×10 ⁻⁴ M	3.3×10 ⁻⁸ M	Brain tissue of rat	(Ledo, Fernandes, Brett, and Barbosa, 2020)
Platinum-black/sealing platinum wires and Prussian blue/sealing platinum wires	Amp	not reported	2.0×10 ⁻⁷ M and 2.1×10 ⁻⁷ M	Blood cells from swine with induced trauma	(Hellmann et al., 2020)
rGO/GO hybrid microelectrode array	Amp	1.0×10 ⁻⁶ to 1.0×10 ⁻³ M	1.8×10 ⁻⁷ M	-	(J. Zhang et al., 2019)
Silver microelectrode array	Amp	0 to 3.7×10 ⁻⁴ M	4.5×10 ⁻⁷ M	-	(Yang et al., 2016)

Table 2.1 Previous research for the electrochemical method for H₂O₂ detection (Continued).

Electrode	Method	Linear range	Limit of detection	Samples	Ref.
Platinum/carbon fiber	CV	4.4×10 ⁻⁵ to 1.2×10 ⁻² M	4.4×10 ⁻⁷ M	U87 cells	(Chen, Li, Jiang, and Wang, 2016)
Platinum-back microelectrode array	Amp	1.0×10 ⁻⁸ to 4.0×10 ⁻⁵ M	1×10 ⁻⁸ M	Mitochondria	(Ben-Amor et al., 2014)
Enzyme/carbon fiber	Amp	5.0×10 ⁻⁵ to 2.5×10 ⁻⁴ M	2.0×10 ⁻⁶ M	Brain slices	(Sanford et al., 2010)
Copper disc microelectrode	Amp	1.5×10 ⁻⁵ to 1.8×10 ⁻³ M	2.8×10 ⁻⁶ M	Whitening commercial products	(Dantas, Castro, Peña, and Bertotti, 2014)
MoS ₂ /GCE	CV	1.0×10 ⁻⁵ to 1.0×10 ⁻⁴ M	1.1×10 ⁻⁵ M	-	(Haritha, Vijayan, Kumar, and Rakhi, 2021)
AuCu/polypyrene /MOF/GCE	SWV	7.1×10 ⁻⁶ to 2.4×10 ⁻² M	6.7×10 ⁻⁶ M	-	(Ma and Zheng, 2020)
PEDOT/Prussian blue /GCE	Amp	5.0×10 ⁻⁷ to 8.4×10 ⁻⁴ M	1.6×10 ⁻⁷ M	Milk	(J. Wang, Wang, Cui, Xu, and Luo, 2017)

2.3 Electrode fabrication: Photolithography

Photolithography is an optical method used to create detailed patterns on a substrate in microscale for microdevice. All the photolithography techniques consist of 3 steps. First, the photosensitive material known as photoresist is spin-coated to cover the substrate. Next, the photomask of pattern is placed on the substrate and then the substrate is exposed to a pattern by intense light. The exposed areas of the photoresist become either more or less soluble in a developer solution, depending on the type of photoresist used. The developer solution is then applied to this substrate to remove unexposed areas of photoresist (Yilbas, Al-Sharafi, and Ali, 2019). The design of microdevice can subsequently be producing the patterned on surface by other technique such as etching, depositing, or sputtering. A schematic diagram of photolithography processes is presented in Figure 2.1.

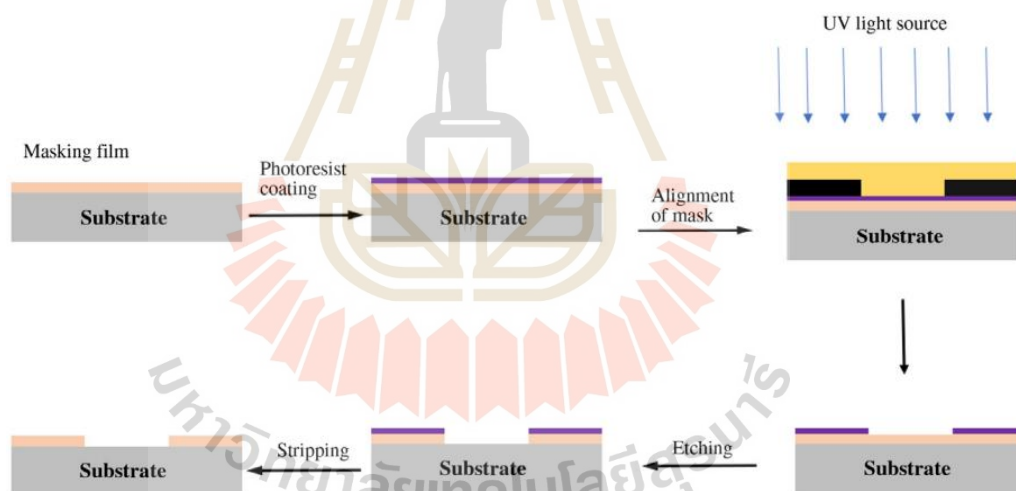


Figure 2.1 Photolithography processes (Yilbas et al., 2019).

Positive and negative photoresists are two types of photoresists that are commonly used in this process. Positive photoresist is a type of photoresist that becomes more soluble in a developer solution when it is exposed to light. When positive photoresist is exposed to the light, the areas of exposition are more soluble in developer solution. On the other hand, when using negative photoresist, the exposed areas are less soluble or insoluble in the developer solution. (Figure 2.2)

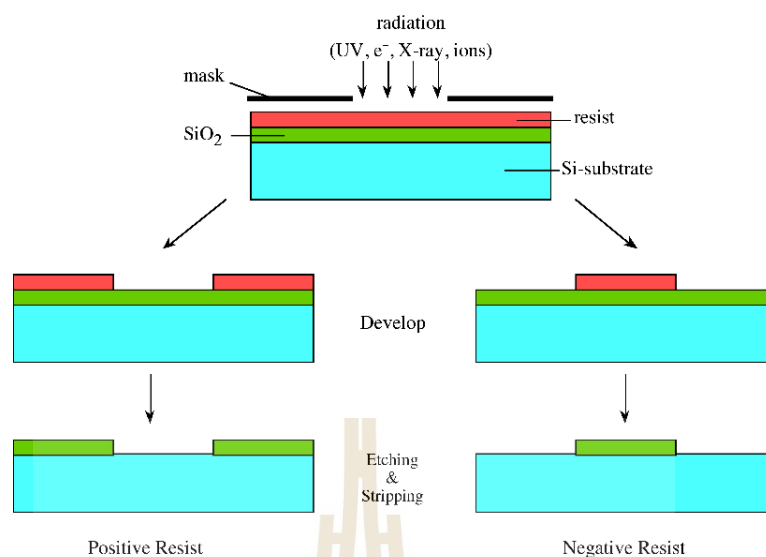


Figure 2.2 Comparison of positive and negative photoresist (Wei).

2.4 Electrode characterization

2.4.1 Cyclic voltammetry

Cyclic voltammetry (CV) is one of the electrochemical techniques which is used widely to investigate the oxidation and reduction processes of redox species. Cyclic voltammetry is invaluable to study electron transfer-initiated chemical reactions. CV is performed by cycling the potential of a working electrode and measuring the current. The applied potential of electrochemical cells is swept linearly with time (Figure 2.3a). The potential in the forward scan reaches at a certain point which is the point where the potential is sufficient to have caused oxidation or reduction of a species of interest. Backward scan potential will get back to the initial potential. The cyclic voltammograms were obtained from the measurement of current of the working electrode during the potential scan. (Figure 2.3b)

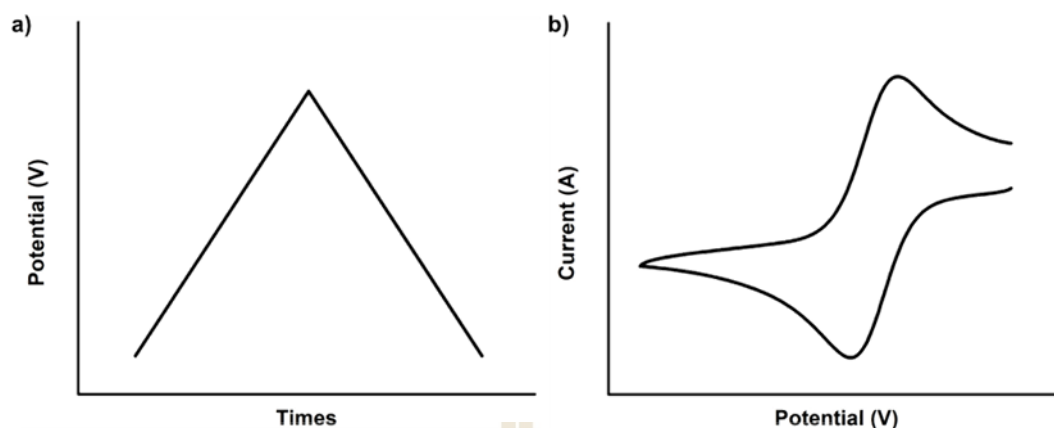


Figure 2.3 a) A plot of the applied potential with time in CV. b) Cyclic voltammogram.

2.4.2 Scanning electron microscope

Scanning electron microscope (SEM) is an electron microscope that uses a focused beam of high-energy electrons to investigate materials instead of light beam because wavelength of electron beam is smaller than light beam. Therefore, SEM has high magnification. A focused beam is utilized in SEM to scan a surface of material and produce a SEM image. The electrons in the beam interact with the materials. SEM image is useful for describing information about the surface morphology of materials.

The principle of SEM is presented in Figure 2.4. The top part of the SEM is an electron gun which is used to produce electrons. Then, an electron moves in the column by accelerating voltage (0.0 – 30.0 kV). Electron mobility and the amount of electrons are controlled by electromagnetic lens and aperture, respectively. The first electron lenses are condenser lenses which are used to define the size of the electron beam from electron source. Objective lenses are the last lens that are used for focusing electron beam to the surface of the material. Objective lenses have a scan coil to help the scanning electrons beam toward the material within the framework. The signal is detected by the detector to create an image in the program.

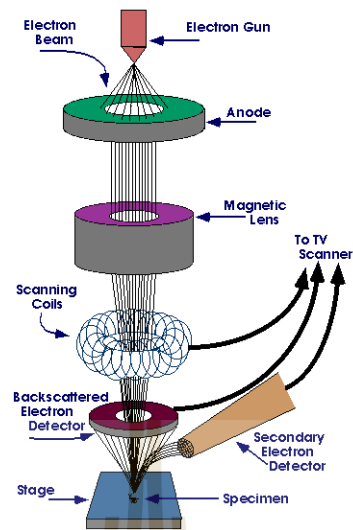


Figure 2.4 Principle of scanning electron microscope (SEM) (Swapp, 2017).

CHAPTER III

THEORY AND SIMULATION

3.1 Fundamentals of electrochemistry

Electrochemistry is the study of chemical reactions which involve electrons transfer processes at an electrode-solution interface.

3.1.1 Equilibrium electrochemistry

Equilibrium electrochemistry is an electrochemistry which deals with electrochemical reactions that occur under conditions of thermodynamic equilibrium. When a metal electrode is immersed in a solution containing redox species A and B, the metal electrode acts as a source or sink of electrons causing oxidation or reduction reaction, refer to equation 3.1.



where A is a oxidizing species, B is a reducing species, and E_f^0 is the formal potential of the reaction.

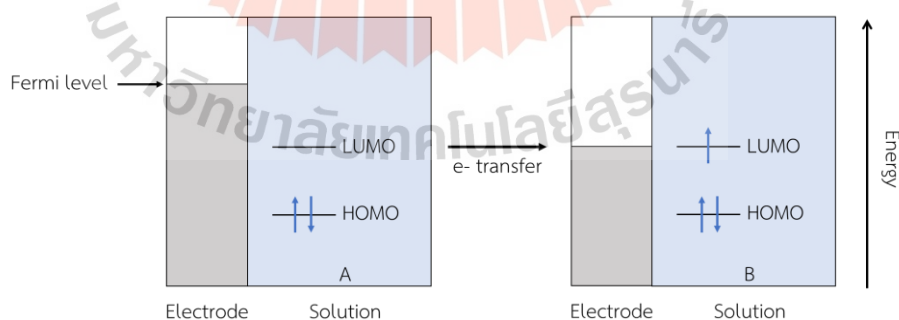


Figure 3.1 Schematic diagram of energy levels of a metal electrode and redox species A and B.

The electron transfer process is shown in Figure 3.1. Electrical charges are accumulated at the electrode/solution interface. The net charge separation at equilibrium between the electrode and the solution phase gives rise to an electrode potential. These relationships are described by the Nernst equation, which relates the electrode potential to the concentrations of the species involved in the reaction.

$$E = E_f^0 + \frac{RT}{F} \ln \left(\frac{c_{A,0}}{c_{B,0}} \right) \quad (3.2),$$

where E is the applied potential, E_f^0 is the standard potential, R is gas rate constant, T is temperature, F is faraday's constant, and C is the concentration at the electrode surface of species i .

This is the Nernst equation used to describe electrochemical equilibrium at the electrode surface.

3.1.2 Dynamic electrochemistry

When applying potential to the electrode, the energy of the Fermi level is disturbed. That makes the rates of oxidation and reduction unequal. If a positive potential is applied, the Fermi level decreases causing electrons transfer from the metal electrode to the solution. The oxidation of B is thus enhanced relative to the reduction of A. If negative potential is applied, the reduction of A is enhanced relative to oxidation of B.

As a result, there is a non-zero net flux of electrons between the electrode and the redox species because the rates of oxidation and reduction are not equal.

The net flux (J) at the electrode is described by equation 3.3.

$$J = k_{red}c_{A,0} - k_{ox}c_{B,0} \quad (3.3),$$

where k_{red} and k_{ox} are the electrochemical rate constant of reduction and oxidation, respectively and $c_{i,0}$ is the concentration at the electrode surface of species i , which may difference from that in the bulk solution.

The number of electrical charges flowing across the entire electrode surface per unit time (current, I) is given by

$$I = FAJ \quad (3.4),$$

where A is the electrode surface area.

Combining equations 3.3 and 3.4, the current is thus calculated by

$$I = FA(k_{red}c_{A,0} - k_{ox}c_{B,0}) \quad (3.5),$$

According to the Butler-Volmer kinetic model (Butler, 1924)

$$k_{red} = k^0 e^{(n-\alpha_c)F\eta} \quad (3.6),$$

$$k_{ox} = k^0 e^{-\alpha_c F\eta} \quad (3.7),$$

where η is the over potential and n is the number of electron transfer.

Therefore,

$$I = nFk_0 \left(c_A e^{\frac{(n-\alpha_c)F\eta}{RT}} - c_B e^{\frac{-\alpha_c F\eta}{RT}} \right) \quad (3.8),$$

This is Butler-Volmer equation which used to predict how current varies as a function of electrical potential (η) and cathodic transfer coefficient (α_c).

3.1.3 Mass transport in solution

When the working electrode is immersed in a stationary solution containing the redox species and excess of supporting electrolyte. The electron transfer reaction takes place on the surface of the working electrode when suitable potential is applied. The redox species can transfer from bulk solution to the electrode surface with three modes mass transport:

- i. Diffusion occurs in all solutions and resulting from concentration gradients. The random movement of species from high concentration to lower concentration.
- ii. Migration is the movement under the electric field gradients.
- iii. Convection is the movement of species by external mechanical force such as stirring or flowing of solution.

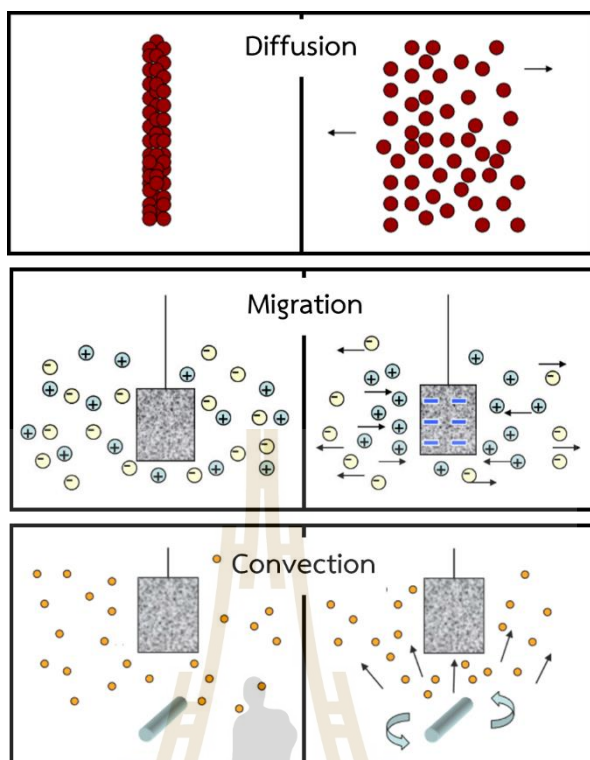


Figure 3.2 Schematic of typical mass transport (Kelly, 2009).

In this thesis, the main mass transport of redox species to the electrode surface is dependent on diffusion. The movement of redox species under the concentration gradient can be described by Fick's law of diffusion.

Fick's 1st law explains how the flux (J) through a unit area in a unit time is related to the concentration gradients (equation 3.9):

$$J = -D\nabla c \quad (3.9),$$

where D is the diffusion coefficient and ∇c is the concentration gradient.

Fick's 2nd law describes the changes in concentrations with time (equation 3.10):

$$\frac{\partial c}{\partial t} = D\nabla^2 c \quad (3.10),$$

where c is the concentration and t is the experiment time.

Consider the linear diffusion in the direction perpendicular (x-axis) to the plane (yz-plane) of area 'A', see Figure 3.3. There is an infinitesimally thin thickness (δx) of solution that including particles (such as ions, molecules) with concentration c_1 and c_2 on the left and the right of the plane, respectively. At the yz-plane, the concentration is constant. The particles are random movement in solution and move across the interest plane with random walk process. The particles have an equal chance to moving to the left and to the right of the compartments. The number of particles moving to the left of the plane is $\frac{c_2 A \delta x}{2}$ and the number of particles moving to the right of the plane is $\frac{c_1 A \delta x}{2}$ in time scale δt .

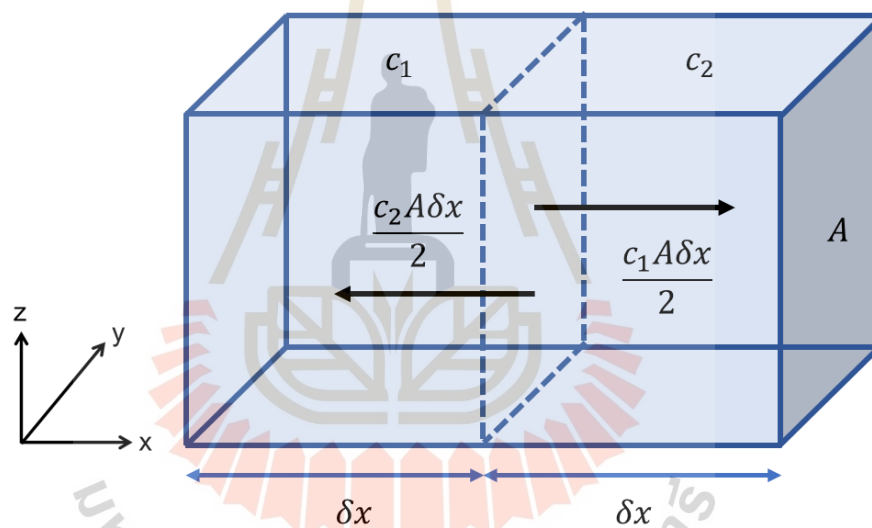


Figure 3.3 The model used in the explanation of Fick's law of diffusion.

The net number of particles (N) passing through a plane of area 'A' in time δt is thus

$$N = \frac{(c_1 - c_2) A \delta x}{2} \quad (3.11),$$

The flux (J) of particles is

$$J = \frac{1}{A \delta t} \frac{A \delta c \delta x}{2} \quad (3.12),$$

where $\delta c = c_1 - c_2$

$$J = \frac{\delta c \delta x}{2 \delta t} \quad (3.13),$$

By multiplying $\delta x / \delta x$ and approximating $\delta c / \delta x$ as $\partial c / \partial x$, eqn. 3.13 can be written as

$$J = - \frac{(\delta x)^2}{2 \delta t} \frac{\partial c}{\partial x} \quad (3.14),$$

The negative sign reflects the movement of particles from high to low concentrations.

From the Einstein-Smoluchowski equation mention the mean-square of the distance ($\langle x^2 \rangle$) travelled by a particle in time t is related to the diffusion coefficient (D) (Bockris, Reddy, and Gamboa-Aldeco, 1998)

$$D = \frac{\langle x^2 \rangle}{2t} = \frac{(\delta x)^2}{2 \delta t} \quad (3.15),$$

Substituting equation 3.14 into equation 3.15 thus yields the Fick's first law as given in equation 3.9, connecting the microscopic random walk process to the macroscopic law of diffusion.

At the beginning of the electrochemical experiment, there is only species A in the entire solution. When a suitable potential is applied, species A is converted to species B at the electrode surface. At the near electrode surface, the concentration of species A decreases, and the concentration of species B increases. Consequently, species A diffuses from the bulk solution to the electrode surface. Species B diffuse away from the electrode surface.

3.2 Electrochemical cell

The electrochemical measurements including the three electrode system (refer to Figure 3.4):

- I. A working electrode (WE) is where the redox reaction of interest takes place.
- II. A counter electrode (CE) is a conductor that completes the cell circuit.
- III. A Reference electrode (RE) is used to measure and control the WE potential.

Cyclic voltammetry is the electrochemical technique that is used in this thesis. In this technique, the potential is applied to the working electrode causing currents of the redox reaction to be measured.

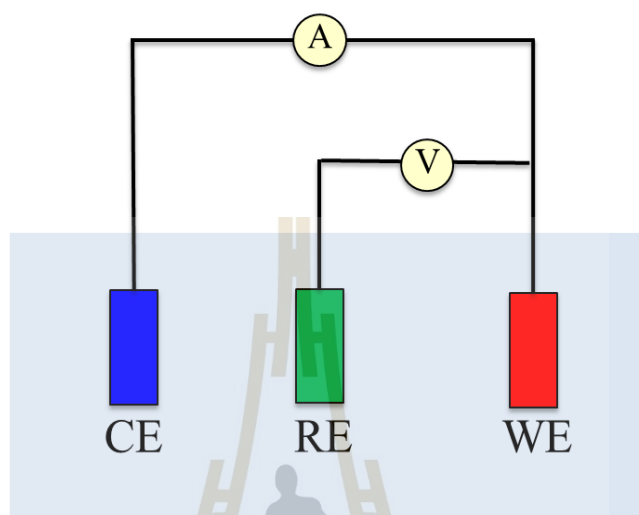


Figure 3.4 An electrochemical three-electrode cell set-up.

3.3 Microelectrode

Microelectrodes have at least one dimension in the order of microns. A microelectrode can be defined as an electrode that has a characteristic surface dimension smaller than the thickness of the diffusion layer on the time scale of the electrochemical experiment. The diffusion regime of microelectrode can be described by two-dimensional (2D) diffusion in which the redox species diffuse from bulk solution to the electrode surface in all directions (Figure 3.5a), in contrast to the diffusion regime of macroelectrode which followed the one-dimensional (1D) diffusion or planar diffusion (Figure 3.5b).

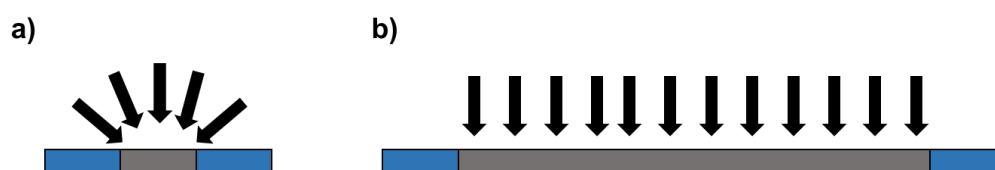


Figure 3.5 Diffusion regime of a) microelectrode and b) macroelectrode.

Microelectrodes allow the measurements in low ionic strength samples (Ngamchuea et al., 2018a, Huang et al., 2009). Reduced Ohmic drop, high current density, high mass transfer flux, low background charging current, and possibilities of *in-vitro* and *in-vivo* applications are strong advantages of microelectrodes (Ngamchuea et al., 2018b, Ngamchuea et al., 2017b). However, low magnitude of currents at a microelectrode (typically pA – nA range) can be easily disturbed by electrical noises. The signals at encapsulated microelectrodes can also be less effective than theoretically predicted due to stray capacitance. A more advanced instrument is thus required to measure the low currents at microelectrodes. These limitations can be overcome by the use of microelectrode arrays which enhance the current responses and sensitivities of the measurements while maintaining the beneficial characteristics of microelectrodes.

The diffusion processes of microelectrode arrays can be grouped into 4 categories (Figure 3.6).

Category 1: the diffusion layer thickness is much smaller than both the electrode width and the separation distance of electrode. The diffusion of the redox species to the electrode is dominated by linear diffusion or planar diffusion.

Category 2: the diffusion layer thickness is higher than the electrodes width. The electrodes are still sufficiently well separated. This regime provides non-linear diffusion or radial diffusion.

Category 3: the separation distance of electrodes is no longer enough to prevent overlap of adjacent diffusion zones.

Category 4: this represents the limiting of category 3 when adjacency diffusion zones overlap to such an extent that the overall concentration profiles is planar.

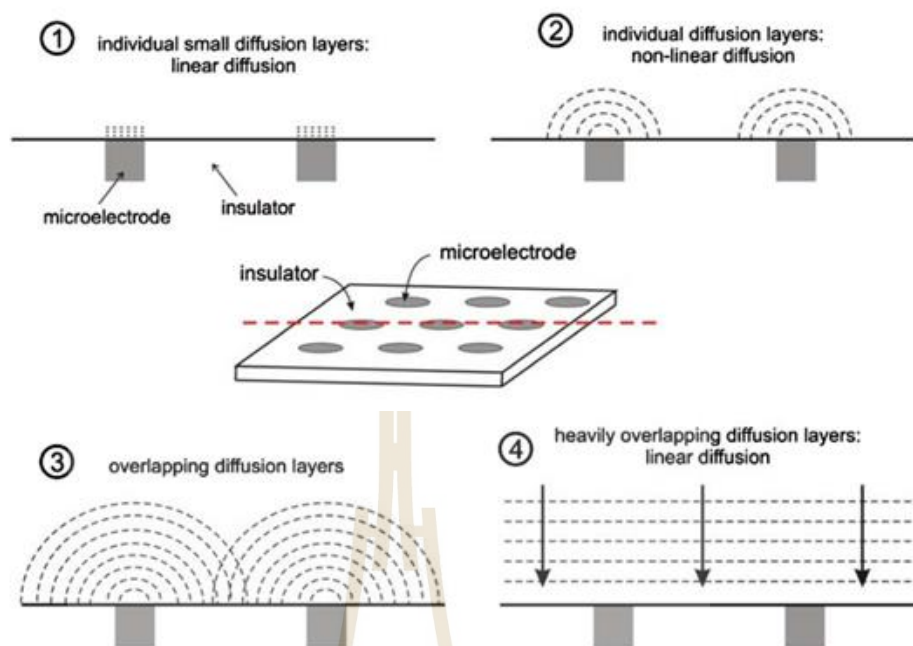


Figure 3.6 Schematic diagram of the four categories of a diffusion process at microelectrode arrays (T. J. Davies and R. G. Compton, 2005).

3.4 Mathematic model and numerical simulation

This section describes the modeling of the simple reduction in equation 3.16 in a cyclic voltammetry at a microband electrodes.



The electron transfer process is described by Butler – Volmer kinetic model at the electrode surface as

$$D \frac{\partial c_A}{\partial x} = nFk_0 \left(c_A e^{\frac{(n-\alpha_c)F\eta}{RT}} - c_B e^{\frac{-\alpha_c F\eta}{RT}} \right) \quad (3.17),$$

At initial condition, only species A in the solution. Thus, concentration of redox species A at the electrode surface is equal to the bulk solution ($c_{A,0} = c_A$). Redox species A occurs the reaction at the electrode surface and redox species A from the bulk solution is diffuse to the electrode surface.

Following the diffusion regime of the microelectrode arrays in categories 1 and 4, the current response is described by linear diffusion or 1D diffusion which is one-dimension problem that easy to solve the problem. The diffusion regime of category 2 is a phenomenon of an isolated microband electrode, which has also been thoroughly investigated and simulated by a variety of two-dimensional approaches. Category 3 is more challenging to solve the two-dimensional problem due to the band is in isolation which diffusion regime is overlap. However, the problem is simplified by identifying diffusionally independent “unit cells” in an approach analogous to that used for microdisc arrays and partially blocked electrodes.

A band of microband electrode arrays have symmetry along with horizontal axis. A symmetry plane is found at the center between two adjacent bands. For all four categories of diffusion regime, there must be a net flux transfer across these surfaces is zero. Therefore, their symmetry plane defines a diffusionally independent unit cell to form the boundaries, which is replicated across the surface of the microelectrode array. Only a one unit cell to be considered for simulation of diffusion to the electrode surface. Figure 3.7 shows a cross section of the unit cell. The width of unit cell is half the electrode size (r) and is half of the electrode separation distance (d).

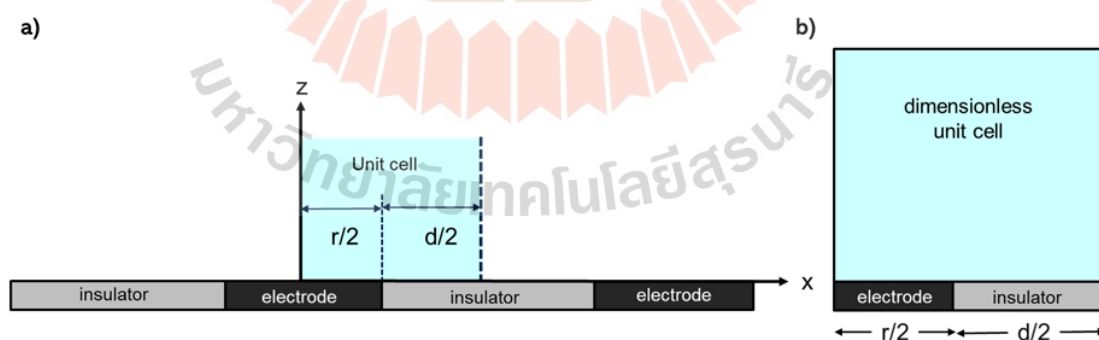


Figure 3.7 a) cross section of the xz plane of the microband electrode. b) unit cell.

The parameters which affect the voltammetric responses at a microband electrode array include the electrode width (r), electrode length (l), electrode separation distance (d), and the height of the connection strip (h) which leads to connection with a potentiostat. The symbols are defined and illustrated in Figure 3.8a.

To evaluate the effects of the designs of microband electrode arrays towards the electrochemical responses, the voltammograms of diffusion-only systems were simulated.

The net flux (J , mol m² s⁻¹) at the electrode was calculated by

$$J = k_{\text{red}}c_{A,0} - k_{\text{ox}}c_{B,0} \quad (3.18),$$

where k_{red} and k_{ox} are the electrochemical rate constants of the reduction and oxidation processes, respectively:

$$k_{\text{red}} = k^0 \exp\left\{\frac{-\alpha F(E - E_f^0)}{RT}\right\} \quad (3.19),$$

$$k_{\text{ox}} = k^0 \exp\left\{\frac{\beta F(E - E_f^0)}{RT}\right\} \quad (3.20),$$

where k^0 is the standard electrochemical rate constant, $c_{i,0}$ is the concentration at the surface of the electrode of species i , and $E - E_f^0$ is the overpotential.

Provided that *diffusion* is the only mode of solution-phase mass transport, the flux of the redox species to the electrode is described by Fick's laws of diffusion:

$$J = -D\nabla c \quad (3.21),$$

$$\frac{\partial c}{\partial t} = D\nabla^2 c \quad (3.22),$$

where J is the flux through a unit area per unit time (mol m⁻² s⁻¹), D is the diffusion coefficient, and ∇c is the local concentration gradient.

The symmetry of the system allows the model to be reduced to 2-dimensional (Streeter et al., 2007). In theory, the voltammetric peak currents thus increase linearly with the length of the electrode (l) and the height of the connection strip (h), provided that the electrode material is sufficiently electrically conductive.

The effects of the electrode width (r) and electrode separation distance (d) are evaluated by simulation using the boundary conditions which are illustrated in Figure 3.8b and described below.

At the insulator surface and the symmetry boundary, the net flux is zero:

$$\left.\frac{\partial c_i}{\partial z}\right|_{z=0} = 0 \quad (3.23),$$

$$\left. \frac{\partial c_i}{\partial x} \right|_{x=0} = 0 \quad (3.24),$$

where c_i is the concentration of species i . x and z are the axes defined in Figure 3.8b.

The height of the simulation space in the z -direction (z_{\max}) must be larger than the distance of the diffusion layer over the timescale of the experiment (t_{\max}) and therefore is set to (R. G. Compton, Laborda, and Ward, 2013):

$$z_{\max} = 6\sqrt{Dt_{\max}}; \quad (3.25),$$

At $z = z_{\max}$, the concentrations of each species are thus equal to their bulk concentrations:

$$c_i(z = z_{\max}) = c_i^* \quad (3.26),$$

Parameter of boundary condition for simulation of cyclic voltammetry at a microband electrode array show in Table 3.1.

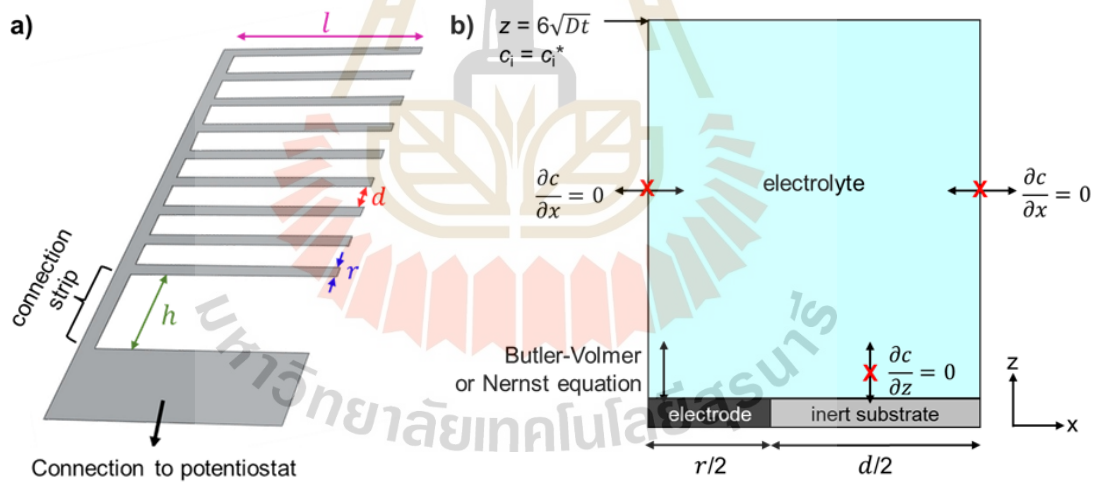


Figure 3.8 a) Illustration of a microband electrode array (MEA) and the definitions of symbols: electrode size (r), electrode separation distance (d), electrode length (l), and height of the connection strip (h). b) Boundary conditions for the simulation of cyclic voltammetry at an MEA in a 2-dimensional unit cell.

Table 3.1 Parameter for boundary conditions.

Parameter	Value
Concentration of species A	1.0 mM
Diffusion coefficient	$1.34 \times 10^{-9} \text{ m}^2/\text{s}$
Time	200 s
Scan rate	0.01 V/s
$Z_{\text{max}} (6\sqrt{Dt})$	3106 μm
k^0 for electrochemical reversible	10^5
k^0 for electrochemical irreversible	10^{-7}
E^0	0.0 V
Potential range	-1.0 V to 1.0 V

3.5 COMSOL Multiphysics

COMSOL Multiphysics is software which is widely used to describe and simulate physics-based processes. It enables the simulation and analysis of the behavior of real-world devices, systems, and physical phenomena under various conditions. The software uses finite element analysis (FEA) and other numerical methods to solve complex problems.

Finite element analysis is the numerical method used to solve partial differential equations (PDEs) that describe physical phenomena such as heat transfer, structural mechanics, and electromagnetics. The concept of FEA is to divide the large pieces into smaller parts with geometric shapes such as triangles, squares, circles and then approximating the solution to the PDE within each element by a simpler function that can be easily computed. The division of the workpiece into smaller pieces in the geometry, or spatial domain, is meshed.

The term "mesh" refers to the discretization of the computational domain into a set of smaller elements or subdomains, which are connected at points called nodes. The accuracy and reliability of the FEA solution depends on the quality and density of the mesh. A finer mesh with more elements can capture the details and complexities

of the system more accurately than a coarser mesh with fewer elements. In this thesis, triangles are used as a mesh to simulate voltammetry shown in Figure 3.9.

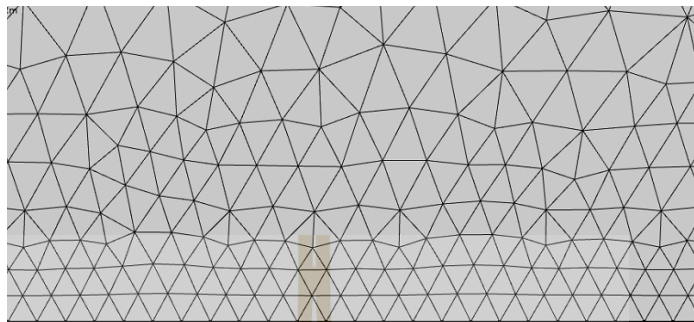


Figure 3.9 An example of triangles mesh.

3.6 Convergence study

Convergence in FEA refers to the state when the solution resolved by the FEA method becomes stable and consistent as the mesh density. The mesh convergence process includes the reduction in the element size and a study of the impact on solution precision. In practical terms, the computation solution of the FEA does not significantly change as the number of elements growth.

In this thesis, the free triangular mesh was used throughout the simulation space with the maximum expansion ratio of 1.1. At the electrode surface, the free triangular mesh was set to be extremely fine with the maximum element size of $r/500$ and the maximum element growth rate of 1.1. The convergence of the chosen spatial and temporal grid sizes was tested by comparing the simulated result with the theoretically predicted peak current at a single microband electrode according to the following equation by Aoki et al. (Aoki and Tokuda, 1987; D. Li, Lin, Batchelor-McAuley, Chen, and Compton, 2019):

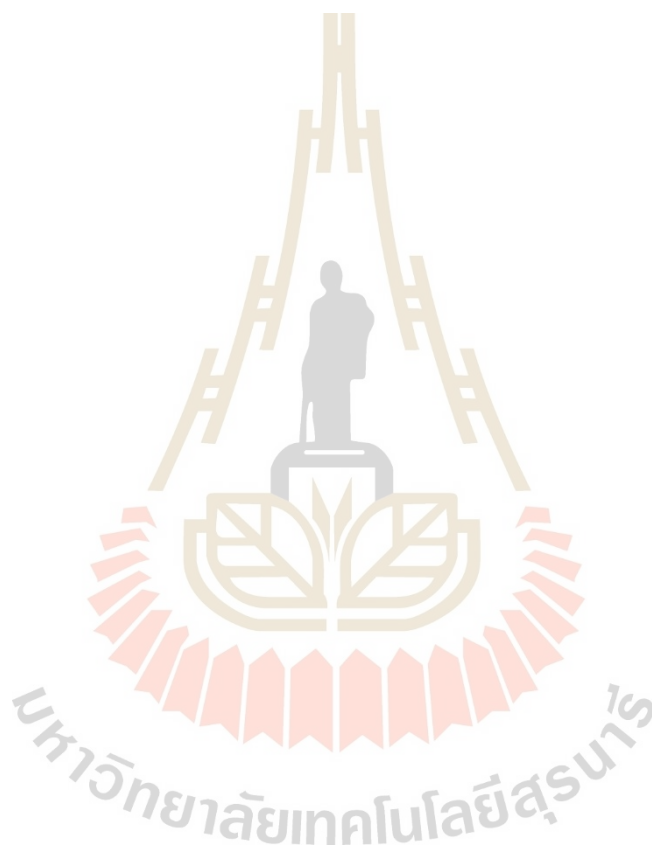
$$\frac{I_p}{nFc^*Dl} = 0.439p + 0.713p^{0.08} + \frac{0.614p}{(1+10.9p^2)} \quad (3.27),$$

where I_p is the voltammetric peak current, n is the number of electrons transferred, F is the Faraday constant ($96,485 \text{ C mol}^{-1}$), c^* is bulk concentration of the redox analyte,

D is the diffusion coefficient, and l is the length of the microband electrode. The parameter p is as follows:

$$p = (nFvr^2/RTD)^{1/2} \quad (3.28),$$

where v is the voltage scan rate, R is the molar gas constant ($8.314 \text{ J K}^{-1} \text{ mol}^{-1}$), and T is the absolute temperature.



CHAPTER IV

EXPERIMENTAL

4.1 Chemical reagents

All chemical reagents were of analytical grades and used as received without any further purification. All solutions were prepared using deionized water (Suranaree University of Technology, Thailand). The chemicals and solvents used in this work as shown in Table 4.1 and Table 4.2.

Table 4.1 List of chemicals used in this work.

Chemical name	Formula	Purity	Sources
Hexaammineruthenium (III) chloride	$\text{Ru(III)(NH}_3)_6\text{Cl}_3$	98%	<i>Thermo Scientific</i>
Hydrogen peroxide	H_2O_2	35%	<i>ANAPURE</i>
Potassium chloride	KCl	$\geq 99\%$	<i>Sigma-Aldrich</i>
Sulfuric acid	H_2SO_4	95 - 97%	<i>Merck</i>
Nitric acid	HNO_3	65%	<i>Merck</i>
Boric acid	H_3BO_3	99.8%	<i>CARLO ERBA Reagents</i>
Potassium hydroxide	KOH	85%	<i>KemAus</i>
Chromium pieces	Cr	99.95%	Kurt J. Lesker Co. Ltd
Silver pieces	Ag	99.99%	Kurt J. Lesker Co. Ltd

Table 4.2 List of chemicals used to prepare synthetic urine (Jiang et al., 2016).

Chemical name	Formula	Concentration	Purity	Sources
Sodium L-lactate	$C_3H_5NaO_3$	11.0 mM	$\geq 99.0\%$	Sigma-Aldrich
Citric acid	$(HOOC(COOH)(CH_2COOH)_2$	2.0 mM	99.5%	QRëC
Sodium hydrogen carbonate	$NaHCO_3$	25.0 mM	99.8%	QRëC
Urea	NH_2CONH_2	170.0 mM	$\geq 99.0\%$	Sigma-Aldrich
Sodium chloride	$NaCl$	90.0 mM	$\geq 99.0\%$	Sigma-Aldrich
Magnesium sulfate	$MgSO_4$	2.0 mM	$\geq 98.0\%$	Tokyo Chemical Industry
Sodium sulfate	Na_2SO_4	10.0 mM	$\geq 99.0\%$	Sigma-Aldrich
Sodium phosphate monobasic	NaH_2PO_4	7.0 mM	$\geq 99.0\%$	Sigma-Aldrich
Sodium phosphate dibasic	Na_2HPO_4	7.0 mM	$\geq 99.0\%$	Sigma-Aldrich
L-ascorbic acid	$C_6H_8O_6$	1.7 mM	$\geq 99.0\%$	Sigma-Aldrich
Dopamine hydrochloride	$(OH)_2C_6H_3CH_2CH_2NH_2 \cdot HCl$	3.0 M	$\geq 97.5\%$	Sigma-Aldrich
Uric acid	$C_5H_4N_4O_3$	2.0 mM	$\geq 99.0\%$	QRëC

Tap water sample was collected onsite at Suranaree University of Technology, Thailand. Drinking water was obtained from Mont Fleur, Saha Pathanapibul Public Company Limited. Milk sample was from Dutch Mill Selected UHT Milk, Dairy Plus Company Limited.

4.2 Electrode fabrication and characterization

The microband electrodes were fabricated by photolithography technique on a glass slide (BOROFLOAT® 33, SCHOTT Technical Glass Solutions GmbH), refer to Figure 4.1. First, the glass slide was cleaned by nitrogen gas and plasma for 10 minutes. The glass slide was spin-coated with positive photoresist (*AZ 1512 HS Photoresist, Microchemicals GmbH*) at 500 rpm for 10 s to spread the photoresist and continue the spin-coating at 3000 rpm for 30 s. Photoresist solvent on a glass slide was evaporated by heat at 90 °C for 90 s. The photoresist was then patterned via UV radiation exposure through a photomask (anti-reflective chrome on soda lime) manufactured by Delta Mask B.V., Netherlands. The electrodes were deposited by e-beam evaporation of 10 nm-thick chromium (Cr) as an adhesion layer followed by 100 nm-thick silver (Ag) on the developed patterns of the photoresist mask in a vacuum: a base pressure of 3×10^{-6} Torr, operating pressures in the range of 8×10^{-6} Torr to 1×10^{-5} Torr, and the maximum currents of 10 mA and 35 mA for Cr and Ag, respectively. Finally, the lift-off process takes place in acetone to remove the photoresist mask.

The size and homogeneity of the microband electrode were analyzed by laser scanning confocal microscope (LSCM, Nikon A1Rsi, Japan). The thickness of the electrode was determined by a 3D optical profiler (Bruker, ContourGT-K (Automated)).

The electrode array consisted of 100 microbands. The width of the microband (r) was either 20 μm or 50 μm . The adjacent electrode separation distance (d) was varied from r to $5r$. The length of the microband (l) was either 2.0 mm or 5.0 mm. The height of the connection strip (h) was either 6.5 mm or 11.7 mm.

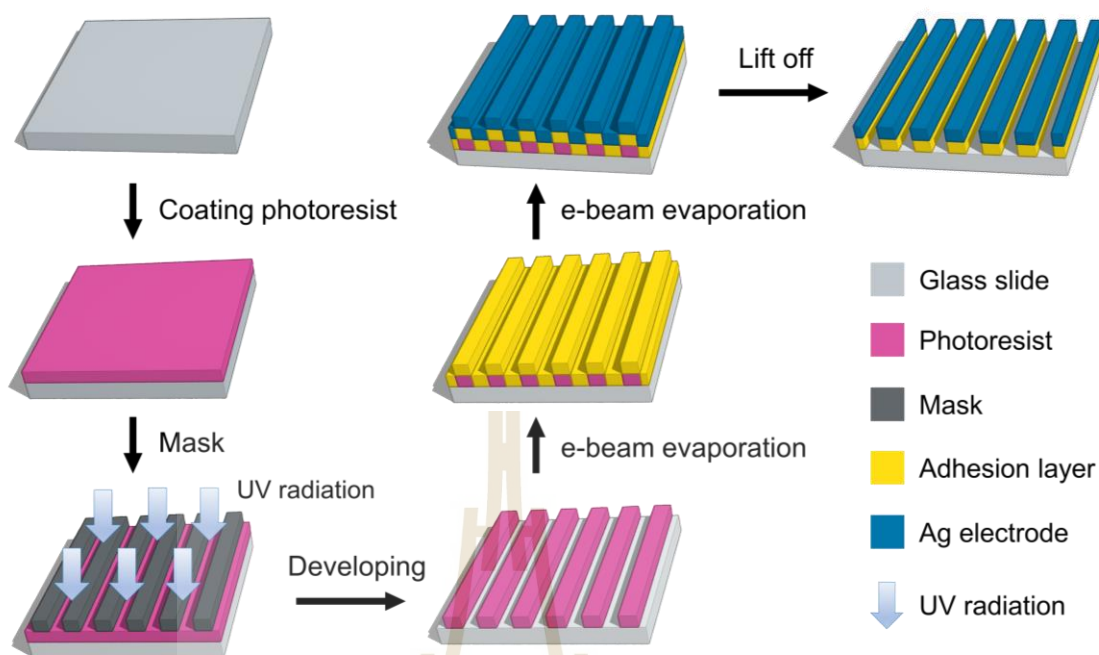


Figure 4.1 Silver microband electrode array (Ag-MEA) fabrication by photolithography.

4.3 Electrochemical measurements

Electrochemical experiments were performed with an Autolab PGSTAT302N potentiostat (Metrohm, Netherlands) using a standard three-electrode setup in a Faraday cage thermostated at 25 °C. A silver microband electrode array (Ag-MEA), a silver/silver chloride (Ag/AgCl in 3.4 M KCl, Italsens), and a platinum sheet were used as working, reference, and counter electrodes, respectively. Before the measurements, Ag-MEA was activated by cyclic voltammetry ($E = 0.0 \text{ V}$ to $+1.0 \text{ V}$ to -0.8 V vs. Ag/AgCl) in 0.10 M KCl at the scan rate of 100 mV s^{-1} . All three electrode systems were immersed in H_2O_2 solution to measure the current signal.

4.4 Application to real sample

The fabricated sensor was applied to direct detection of H_2O_2 in various real samples such as synthetic urine, tap water, drinking water, and milk sample using the standard addition method. 5.0 mM of H_2O_2 in samples used as stock solution. The

standard solution and samples were prepared without the addition of supporting electrolyte as shown in Table 4.3.

Table 4.3 Preparation of sample and standard solution.

Solution	Stock solution (mL)	Sample (mL)
Sample	0.00	10.00
0.25 mM standard H ₂ O ₂	0.50	9.50
0.50 mM standard H ₂ O ₂	1.00	9.00
1.00 mM standard H ₂ O ₂	2.00	8.00
1.50 mM standard H ₂ O ₂	3.00	7.00
2.00 mM standard H ₂ O ₂	4.00	6.00

All of the solutions were measured for their current signal using cyclic voltammetry. A graph of peak current versus the added analyte concentration (i.e., the concentration of the standard minus 0.25 mM H₂O₂, which was used as the spiked concentration) was plotted. The intercept of the curve gives the signal of the sample in the absence of added analyte.

CHAPTER V

RESULTS AND DISCUSSION

5.1 Simulation results

The parameter which affects the voltammetric responses at a microband electrode array include the electrode width (r), electrode length (l), and electrode separation distance (d). The effect of parameter was investigated by simulation in this section.

Figures 5.1a and 5.1b demonstrate the simulated voltammograms at varied r and d for electrochemically reversible (fast electron-transfer kinetics) and irreversible processes (slow electron-transfer kinetics), respectively. In both cases, the voltammetric peak current densities (i_p) increase with the electrode separation distances and then reach a maximum value (a theoretically predicted value for a single microband electrode) at sufficiently large distance ($d/r \sim 10$ for the employed conditions), refer to the inlays in Figures 5.1a and 5.1b. Examples of the concentration profiles at the potential $E - E_0 = 0$ V are shown in Figure 5.1c (reversible, $k^0 = 10^5$) and Figure 5.1d (irreversible, $k^0 = 10^{-7}$). At short electrode separation distances (e.g. $d/r = 1$), the diffusion layers strongly overlap, resulting in mainly planar or 1D diffusion which lower the mass transport efficiency. At wider electrode separation (large d/r values), the diffusion becomes convergent with a small extent of overlapping, and hence give rise to higher current density.

The simulation results show that if considering only the current density, it is preferable to use microelectrode arrays with large separation distances. However, in practice, we need to compromise between the current density, the total current, the use of space and correspondingly the amount of sample required to cover the electrode in the analysis, while also trying to maintain the advantageous characteristics of microelectrode that is the lower requirement of supporting electrolyte. This will be further investigated by experimental studies in the following sections.

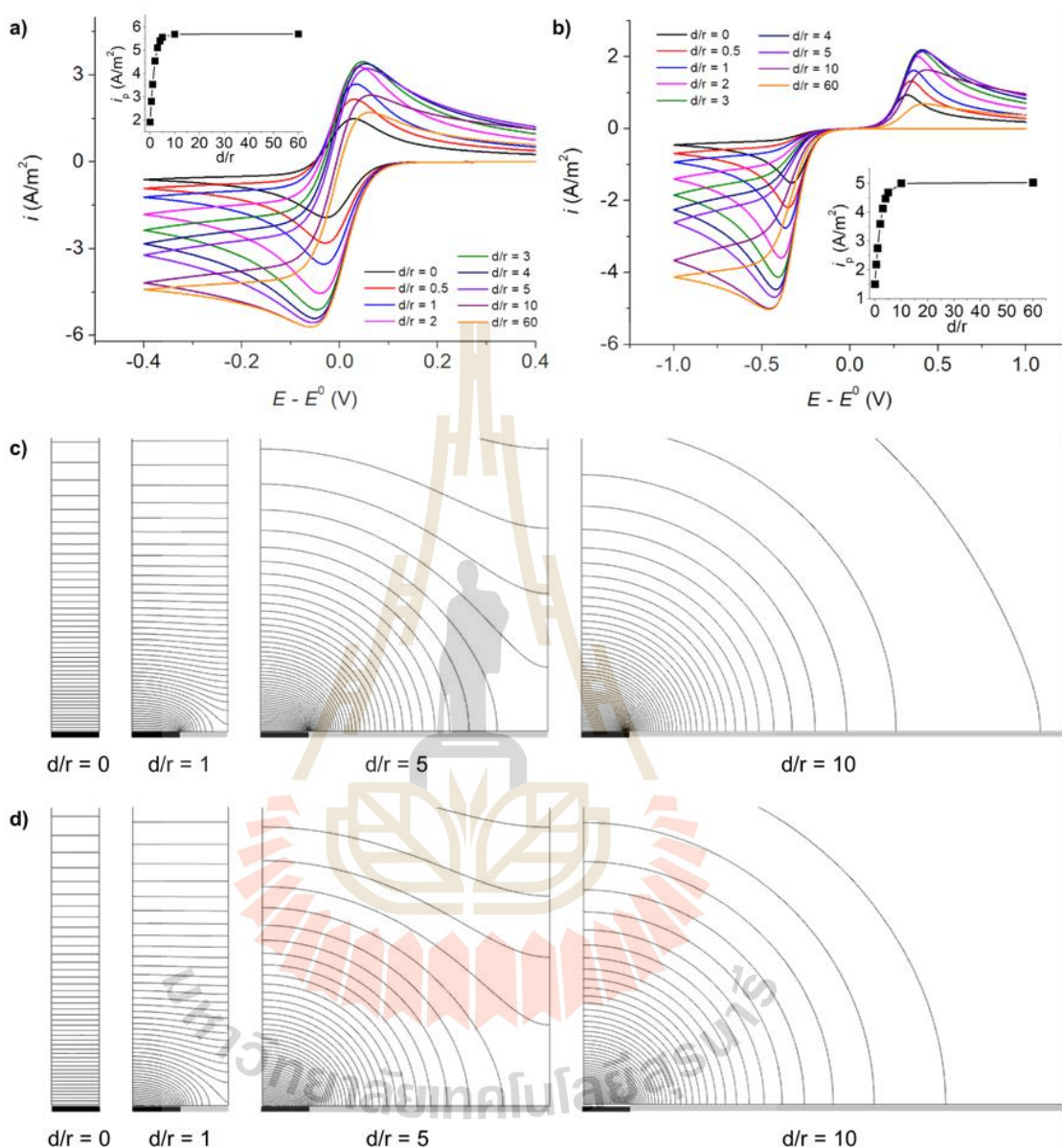


Figure 5.1 Simulated cyclic voltammograms at microband electrode array in 2D simulation space of a 1-electron process ($A + e^- \rightleftharpoons B$): a) Reversible ($k^0 = 10^5$), and b) Irreversible ($k^0 = 10^{-7}$). Concentration profiles at $E - E_0 = 0$ V of A: c) Reversible ($k^0 = 10^5$), and d) Irreversible ($k^0 = 10^{-7}$). $r = 20 \mu\text{m}$, $v = 50 \text{ mV s}^{-1}$, $\alpha = 0.5$, $T = 298 \text{ K}$, $D_A = D_B = 10^{-9} \text{ m}^2 \text{ s}^{-1}$, $c_A^* = 1 \text{ mol m}^{-3}$, $c_B^* = 0 \text{ mol m}^{-3}$. \blacksquare : Electrode. \blacksquare : Insulator. The images are in proportional scale.

5.2 Cyclic voltammetry of H₂O₂ at Ag macroelectrode

First, the Ag macrodisc electrode (diameter = 2.0 mm) was subjected to voltammetric measurements in 10.0 mM H₂O₂ in the presence of 0.10 M KCl at the scan rate of 10 mV s⁻¹. Tafel analysis (equation 5.1) using currents in the range of 15 – 50% of the peak currents (to avoid the influence of diffusional mass transport) revealed the cathodic transfer coefficient (α) of H₂O₂ at an Ag macroelectrode to be 0.47 ± 0.02 (and hence $n' = 0$), refer to Figure 5.2a.

$$\frac{\partial \ln I}{\partial E} = \frac{(n' + \alpha_{n+1})F}{RT} \quad (5.1),$$

where I is the electrical current, E is the applied potential, n is the number of electrons transferred before the rate determining electron transfer step (RDS), α_{n+1} is the cathodic transfer coefficient of the RDS, R is the molar gas constant (8.314 J K⁻¹ mol⁻¹), T is the absolute temperature (298 K), and F is the Faraday constant (96,485 C mol⁻¹) (Batchelor-McAuley and Compton, 2012; Richard G Compton and Banks, 2011).

The voltammetry of H₂O₂ was next performed at varied scan rates (Figure 5.2b). The analysis of the linear dependence of the H₂O₂ cathodic peak currents with \sqrt{v} according to equation 5.2 yielded the diffusion coefficient of H₂O₂ of $1.44 \times 10^{-9} \pm 0.02 \times 10^{-9} \text{ m}^2 \text{ s}^{-1}$.

$$I_p = 0.496 \sqrt{n' + \alpha_{n+1}} n F A c^* \sqrt{\frac{FvD}{RT}} \quad (5.2),$$

given that $\alpha_{n+1} = 0.47$, $n' = 0$, $n = 2$, c^* is the bulk concentration of H₂O₂ ($c^* = 10.0$ mM), A is the electrode surface area ($A = 7.07 \times 10^{-6} \text{ m}^2$), $R = 8.314 \text{ J K}^{-1} \text{ mol}^{-1}$, $T = 298$ K.

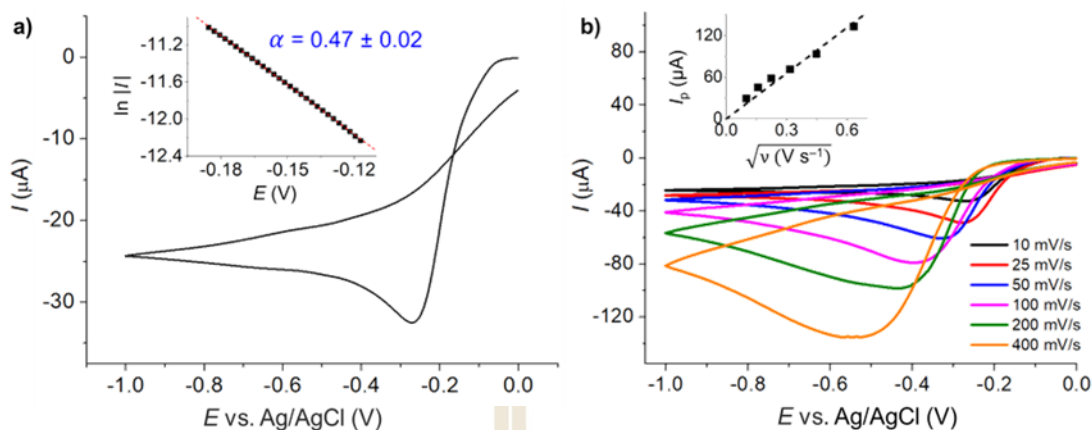


Figure 5.2 a) CV of 10.0 mM H₂O₂ in 0.10 M KCl at Ag macroelectrode (2.00 mm diameter) at the scan rate of 10 mV s⁻¹. The inset shows the plot of ln |*I*| vs. *E* in Tafel analysis. b) CV of 10.0 mM H₂O₂ in 0.10 M KCl at varied scan rates. The inset shows the plot of peak potentials (*I*_p) vs. square root of scan rates (√*v*).

5.3 Characterization of Ag microband electrode arrays (Ag-MEA)

Next, silver microband electrode arrays (Ag-MEA) were fabricated for H₂O₂ detection. The successful adhesion of silver to the substrate and the homogeneity of the electrode sizes and separation distances of the fabricated Ag-MEAs were confirmed by confocal microscopic images in Figure 5.3. The actual sizes of the electrodes were summarized in Table 5.1. The morphology of the Ag-MEA was studied by scanning electron microscope (Figure 5.3m). Homogeneous distribution of spherical silver grains (13.5 – 5.7 nm diameter) was observed throughout the electrode surface. The thickness of the chromium adhesion layer and the silver electrode layer were determined to be 10 nm and 100 nm, respectively. The employed thickness has been reported to yield electrical conductivity close to that of a bulk silver (ca. 4 × 10⁻⁸ Ωm) (Shiva, Ayachit, and Udachan, 2019) and give rise to reproducible and well-defined voltammograms, presented in the later sections.



Figure 5.3 Microscopic images of Ag-MEA with $r = 20 \mu\text{m}$ (a-e) at different electrode separation distances: a) $d = 20 \mu\text{m}$, b) $d = 40 \mu\text{m}$, c) $d = 60 \mu\text{m}$, d) $d = 80 \mu\text{m}$, e) $d = 100 \mu\text{m}$. f) Photo of an Ag-MEA ($r = 20 \mu\text{m}, d = 20 \mu\text{m}$). Microscopic images of Ag-MEA with $r = 50 \mu\text{m}$ (g-k) at different electrode separation distances: g) $d = 50 \mu\text{m}$, h) $d =$

100 μm , i) $d = 150 \mu\text{m}$, j) $d = 200 \mu\text{m}$, k) $d = 250 \mu\text{m}$. l) Photo of an Ag-MEA ($r = 50 \mu\text{m}$, $d = 50 \mu\text{m}$) and m) SEM images of the Ag-MEA ($r = 20 \mu\text{m}$, $d = 20 \mu\text{m}$) at different magnification.

Table 5.1 Measured sizes of the fabricated Ag-MEAs.

r (μm)	d (μm)	Measured r (μm)	Measured d (μm)
20	20	19.50 ± 0.13	20.78 ± 0.20
20	40	20.64 ± 0.17	39.83 ± 0.30
20	60	20.28 ± 0.88	60.10 ± 0.57
20	80	20.52 ± 0.64	80.03 ± 0.51
20	100	20.24 ± 0.36	100.27 ± 0.51
50	50	51.36 ± 0.28	49.14 ± 0.29
50	100	49.90 ± 0.34	99.93 ± 0.72
50	150	49.86 ± 0.46	148.90 ± 0.46
50	200	49.91 ± 0.40	199.98 ± 0.72
50	250	50.48 ± 0.83	249.94 ± 1.66

5.4 Requirement of adhesion layer and electrode activation

Due to the poor adhesion between silver and the glass substrate, an adhesion layer is required. The two common adhesion materials, chromium and titanium, were tested. Figure 5.4a showed that there was no significant difference in the voltammetric responses caused by the adhesion layer. Chromium was thus chosen for the production of Ag-MEA due to its lower cost.

The electrodes showed poor electroactivity without electrode activation possibly due to contamination from organic solvents used in the washing and cutting processes in mass production of the electrodes. The optimal activation procedure

which yielded reproducible well-defined voltammograms with high current densities was done by the voltammetric oxidation [$\text{Ag}_{(s)} \rightarrow \text{Ag}^+_{(aq)} + e^-$] and re-deposition [$\text{Ag}^+_{(aq)} + e^- \rightarrow \text{Ag}_{(s)}$] of the electrode which can be performed in a blank 0.10 M KCl electrolyte or directly in the tested H_2O_2 sample, as shown in the inlay of Figure 5.4b.

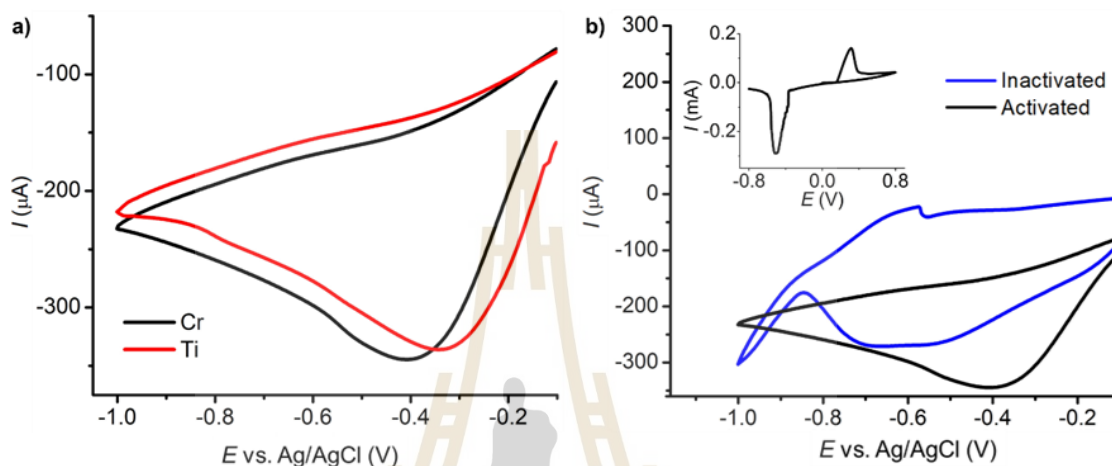


Figure 5.4 CV of 10.0 mM H_2O_2 in 0.10 M KCl at the scan rate of 50 mV s^{-1} at Ag MEA ($r = 50 \mu\text{m}$, $d = 100 \mu\text{m}$, $l = 2 \text{ mm}$). a) Different adhesion layers: Ti (red) vs. Cr (black). b) Without activation (blue) vs. With activation (black). The inlay in b) shows the stripping and re-deposition of Ag in the activation of the electrode.

5.5 Effects of electrode size (r), separation distance (d), length (l), and height (h)

The current densities at Ag-MEA were higher than that measured at an Ag-macroelectrode (e.g. $i_p = 25.7 \text{ A m}^{-2}$ at Ag-MEA ($r = 20 \mu\text{m}$, $d = 20 \mu\text{m}$, $l = 2 \text{ mm}$, $h = 6.5 \text{ mm}$) vs. $i_p = 20.5 \text{ A m}^{-2}$ at Ag-macroelectrode for $[\text{H}_2\text{O}_2] = 10.0 \text{ mM}$) due to the more efficient diffusion of the redox analyte to the electrode surface. These current densities at Ag-MEA depend on several parameters such as electrode size (r), separation distance (d), length (l), and height (h).

Figure 5.5a compares the voltammograms of 10.0 mM H_2O_2 at different electrode separation distances ($d = 50, 100, \text{ or } 150 \mu\text{m}$ for $r = 50 \mu\text{m}$, $l = 2 \text{ mm}$, $h = 6.5 \text{ mm}$). The peak currents increased with increasing separation distances due to less

overlap of diffusion layers resulting in more efficient diffusion of H_2O_2 to the electrode surface.

Figure 5.5b demonstrates the effects of the electrode width (r). At the small separation distance ($r = d$), the peak current densities of $r = 20 \mu\text{m}$ and $r = 50 \mu\text{m}$ were not significantly different due to strong overlap of the diffusion layers resulting in the voltammogram which closely resembled that of a macroelectrode. At larger separation distances, the peak current densities at $r = 20 \mu\text{m}$ were higher than that at $r = 50 \mu\text{m}$ due to the more convergent nature of the diffusion regime of the former.

The effects of the length of the electrodes (l) and the height of the connection strip (h) are demonstrated in Figures 5.5c and 5.5d, respectively. The peak current densities are *not* significantly affected by the parameters l and h , as theoretically predicted. The results further confirmed that the fabricated electrodes were sufficiently electrically conductive such that the voltammograms were not significantly altered when the values of l and h changed, provided that the area of the electrode which is exposed to the solution is controlled.

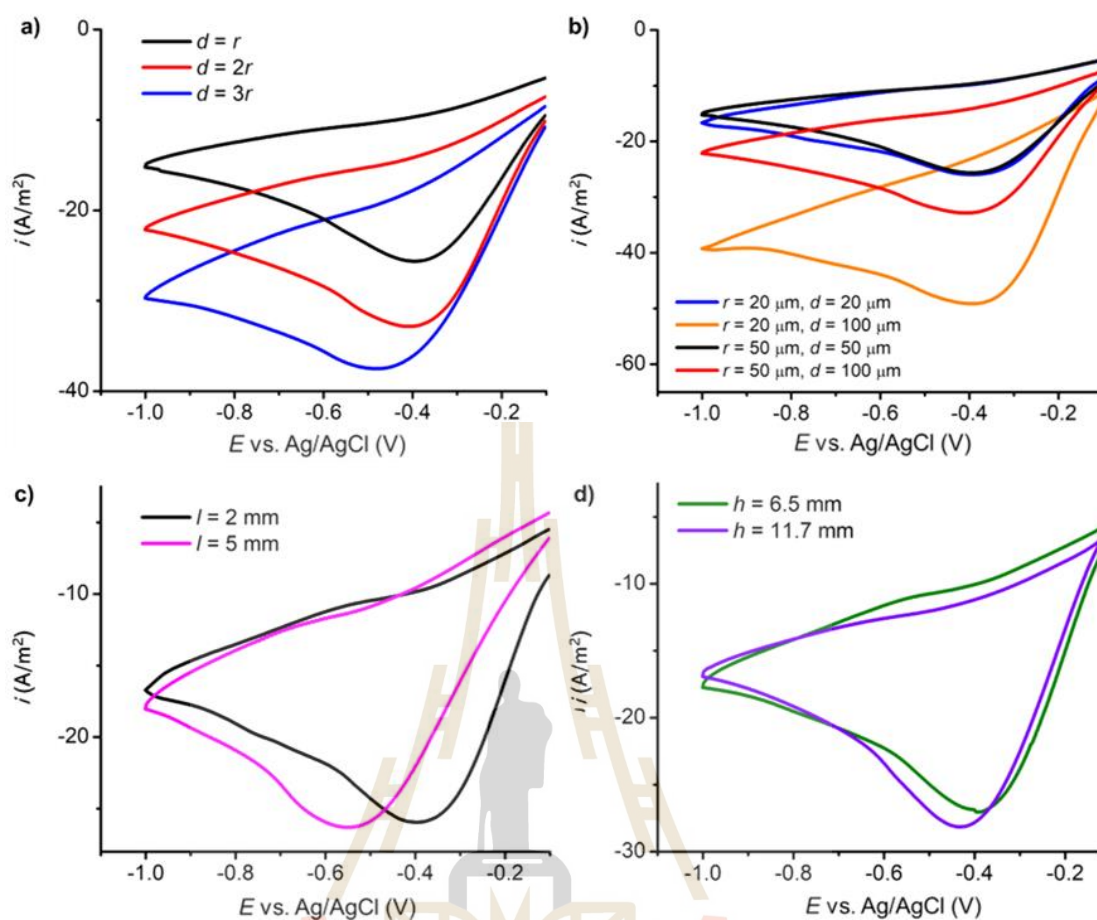


Figure 5.5 CV of 10.0 mM H_2O_2 in 0.10 M KCl at the scan rate of 50 mV s^{-1} at silver microband electrodes with a) different d : (black) $50 \mu\text{m}$, (red) $100 \mu\text{m}$, (blue) $150 \mu\text{m}$; fixed $r = 50 \mu\text{m}$, $l = 2.00 \text{ mm}$, $h = 6.5 \text{ mm}$. b) different r : $r = 20 \mu\text{m}$, $d = 20 \mu\text{m}$ vs. $r = 50 \mu\text{m}$, $d = 50 \mu\text{m}$ vs. $r = 20 \mu\text{m}$, $d = 100 \mu\text{m}$ vs. $r = 50 \mu\text{m}$, $d = 100 \mu\text{m}$. c) different l : (black) $l = 2.00 \text{ mm}$ vs. (pink) 5.00 mm (fixed $r = 20 \mu\text{m}$, $d = 20 \mu\text{m}$, $h = 6.5 \text{ mm}$). d) different h : (black) $h = 6.5 \text{ mm}$ vs. (yellow) $h = 11.7 \text{ mm}$.

In addition to the currents and current densities, in practice we need to consider the amount of sample required in the analysis. The sample volumes of ca. 5, 13, and $20 \mu\text{L}$ are required to cover the Ag-MEAs (100-band, $r = 20 \mu\text{m}$) with $d = 20$, 40, and $60 \mu\text{m}$, respectively. Meanwhile, ca. 25, 40, and $50 \mu\text{L}$ are required to cover the Ag-MEAs (100-band, $r = 50 \mu\text{m}$) with $d = 50$, 100, and $150 \mu\text{m}$, respectively. Due to the small volume required and its sufficient ability to detect H_2O_2 in complex samples (demonstrated in the later section), we chose the Ag-MEA with $r = 20 \mu\text{m}$ and $d = 20$

μm as a paradigmatic example to demonstrate the advantages of microelectrode arrays in H_2O_2 detection. The analytical performances of this electrode were investigated next.

5.6 Reproducibility tests

The reproducibility was tested for both within (intra) and between (inter) electrodes. The relative standard deviation (RSD) of voltammetric peak currents at an Ag-MEA ($r = 20 \mu\text{m}$, $d = 20 \mu\text{m}$, $l = 2 \text{ mm}$, $h = 6.5 \text{ mm}$) of $10.0 \text{ mM H}_2\text{O}_2$ was 1.20% ($n = 5$), indicating excellent repeatability within the electrode. The Ag-MEA electrode can be used up to 10 times with $\text{RSD} < 5\%$ and the electrode activation is only required once before the first use. The measurements of $10.0 \text{ mM H}_2\text{O}_2$ at five different Ag-MEA electrodes of the same size yielded the relative standard deviation (RSD) of 1.12% ($n = 5$), demonstrating excellent reproducibility between electrodes.

5.7 Calibration curve

Figure 5.6 shows cyclic voltammograms of varied concentrations of H_2O_2 in 0.10 M KCl at an Ag-MEA ($r = 20 \mu\text{m}$, $d = 20 \mu\text{m}$, $l = 2 \text{ mm}$, $h = 6.5 \text{ mm}$) at the scan rate of 50 mV s^{-1} . The linear range, sensitivity, and limit of detection were determined to be $0.0 - 10.0 \text{ mM}$, $9.84 \pm 0.34 \mu\text{A mM}^{-1}$, and $22.69 \mu\text{M}$, respectively.

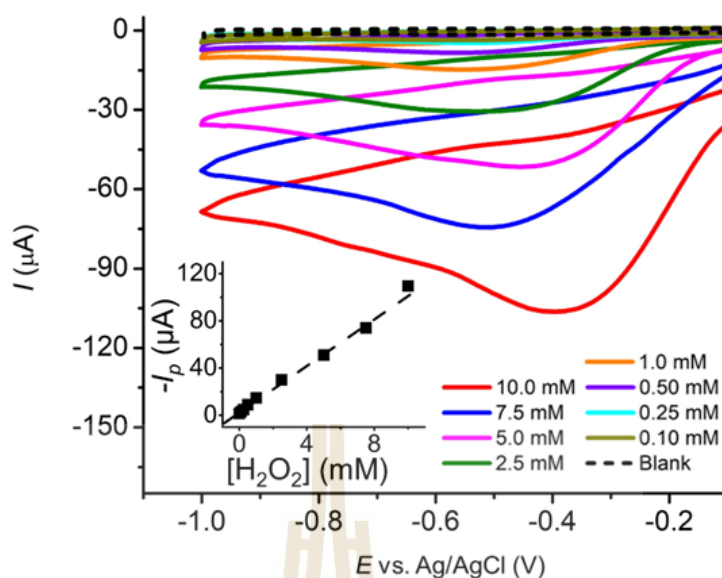


Figure 5.6 CV of varied concentrations of H_2O_2 at the scan rate 50 mV s^{-1} . Ag-MEA ($r = 20 \text{ }\mu\text{m}$, $d = 20 \text{ }\mu\text{m}$, $l = 2 \text{ mm}$, $h = 6.5 \text{ mm}$) in 0.10 M KCl .

5.8 Applications in synthetic urine, tap water, drinking water, and milk samples

The developed method was applied in the direct analysis of H_2O_2 in synthetic urine, tap water (Suranaree University of Technology, Thailand), drinking water (Mont Fleur, Saha Pathanapibul Public Company Limited), and milk samples (Dutch Mill Selected UHT Milk, Dairy Plus Company Limited) without dilution or addition of supporting electrolyte. The proposed method was evaluated by spiking and recovery tests (standard addition) of $250.0 \text{ }\mu\text{M H}_2\text{O}_2$ in the samples. The spiked samples were subjected to cyclic voltammetry at an Ag-MEA electrode ($r = 20 \text{ }\mu\text{m}$, $d = 20 \text{ }\mu\text{m}$, $l = 2 \text{ mm}$, $h = 6.5 \text{ mm}$) at the scan rate of 50 mV s^{-1} . The observed % recoveries were 97.6% (RSD = 4.4%), 97.7% (RSD = 3.6%), 98.6% (RSD = 2.4%), and 95.8% (RSD = 2.5%) in synthetic urine, tap water, drinking water, and milk samples, respectively. The $\sim 100\%$ recoveries showed that the fabricated electrodes and the developed method exhibited excellent tolerance to interferences present in the synthetic urine, tap water, drinking water, and milk samples.

Table 5.2 Spike and recovery tests of H_2O_2 in synthetic urine, tap water, drinking water, and milk samples.

Sample	H_2O_2 added (μM)	H_2O_2 found (μM)	RSD (%)	Recovery (%)
Synthetic urine	250.0	244.0	4.4	97.6
Tap water	250.0	244.3	3.6	97.7
Drinking water	250.0	246.5	2.4	98.6
Milk	250.0	239.6	2.5	95.8

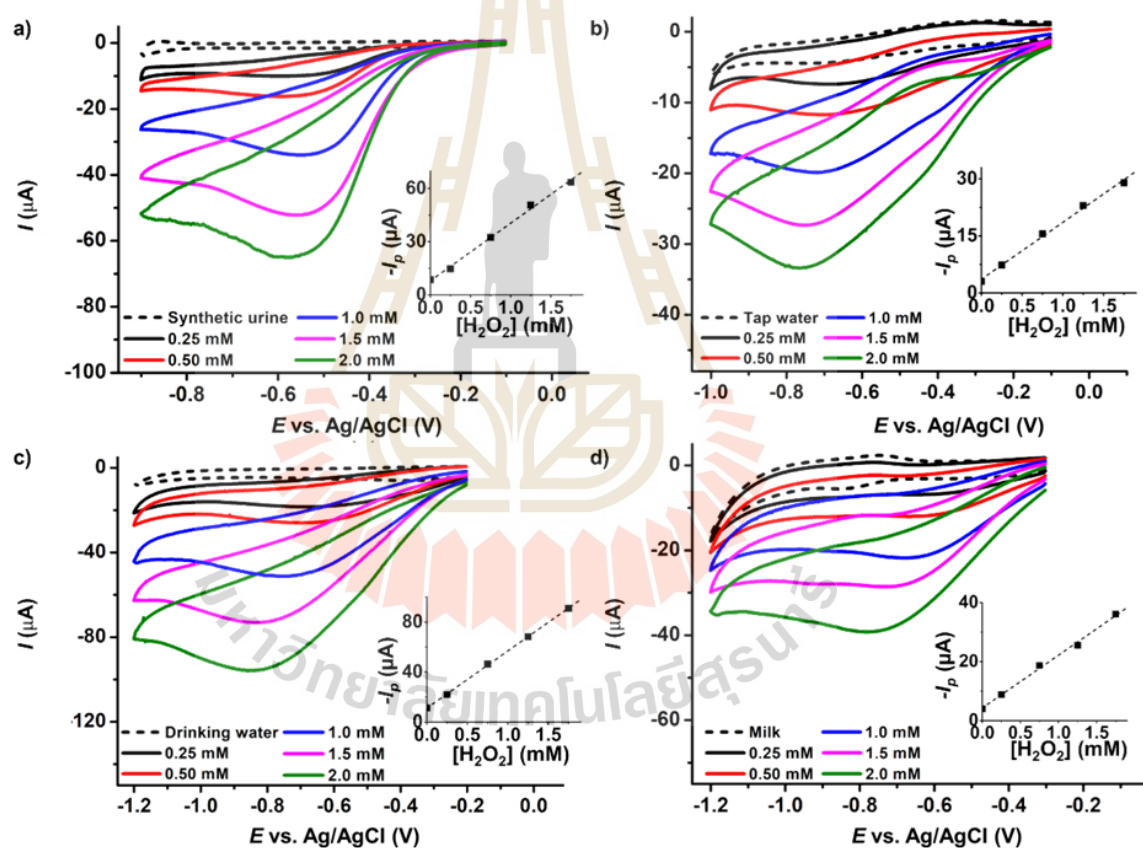
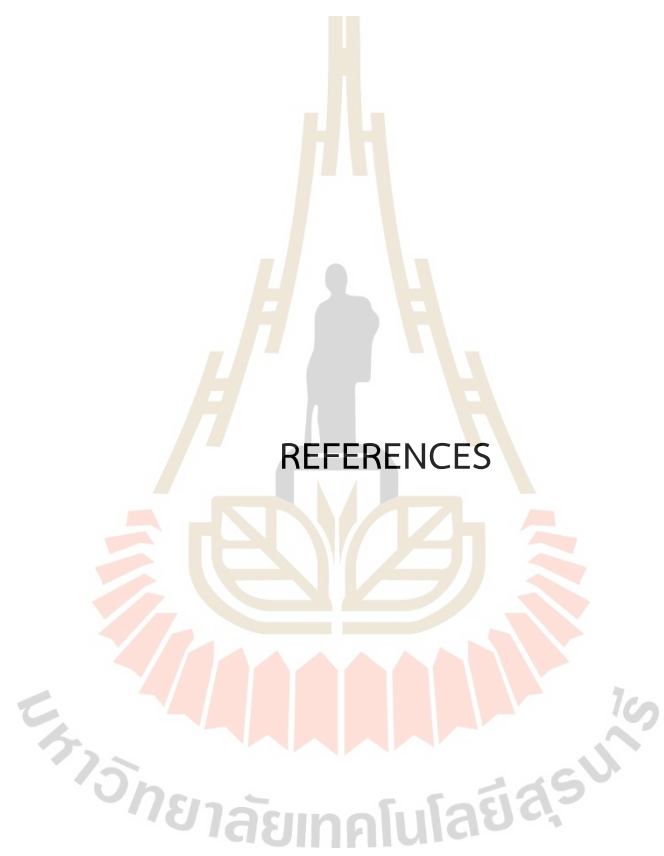


Figure 5.7 Cyclic voltammograms of a) synthetic urine, b) tap water, c) drinking water, and d) milk spiked with different concentrations of H_2O_2 in the recovery studies by standard addition method at an Ag-MEA electrode at the scan rate of 50 mV s^{-1} .

CHAPTER VI

CONCLUSION

In this work, we fabricated silver microband electrode arrays (Ag-MEA) by photolithography technique for a one-step analysis of H_2O_2 without dilution of sample or addition of supporting electrolyte. A more efficient mass transport to the microelectrode surface resulted in large current densities and lowered the requirement of electrolytic support, allowing direct detection of H_2O_2 in the samples. The fast (ca. 36 s) and simple sensor is convenient and easy to use which can facilitate routine testing of H_2O_2 . The effects of the electrode width, band-to-band separation, electrode length, and the height of the connection strip towards the voltammetric responses of H_2O_2 were evaluated. The developed sensor showed excellent reproducibility, sensitivity, and limit of detection. The sensor was tested in the presence of various interfering species present in synthetic urine, tap water, drinking water, and milk samples. The ~100% recovery indicated high selectivity of the sensor and the robustness of the Ag-MEA electrodes. This shows that the sensor can be potentially used for the analysis of H_2O_2 which is an important biomarker of oxidative stress in biological fluids as well as the detection of H_2O_2 in food and environmental samples. The successful application of the sensor in milk further highlighted the advantage of electrochemical measurement in the analysis of opaque samples.



REFERENCES

REFERENCES

- Abdollahi, M., and Hosseini, A. (2014). Hydrogen peroxide. *Encyclopedia of Toxicology*, 3, 967-970.
- Aoki, K., and Tokuda, K. (1987). Linear sweep voltammetry at microband electrodes. *Journal of Electroanalytical Chemistry and Interfacial Electrochemistry*, 237(2), 163-170.
- Arefin, S., Sarker, M. A. H., Islam, M. A., Harun-ur-Rashid, M., and Islam, M. N. (2017). Use of Hydrogen Peroxide (H₂O₂) in raw cow's milk preservation. *Journal of Advanced Veterinary and Animal Research*, 4(4), 371-377.
- Barnes, E. O., Fernandez-la-Villa, A., Pozo-Ayuso, D. F., Castano-Alvarez, M., and Compton, R. G. (2015). Validating the geometry of interdigitated band electrodes: A variable scan rate study. *Journal of Electroanalytical Chemistry*, 748, 82-90.
- Batchelor-McAuley, C., and Compton, R. G. (2012). Voltammetry of multi-electron electrode processes of organic species. *Journal of Electroanalytical Chemistry*, 669, 73-81.
- Ben-Amor, S., Vanhove, E., Belaïdi, F. S., Charlot, S., Colin, D., Rigoulet, M., Launay, J and Temple-Boyer, P. (2014). Enhanced detection of hydrogen peroxide with platinumized microelectrode arrays for analyses of mitochondria activities. *Electrochimica Acta*, 126, 171-178.
- Bockris, J. O. M., Reddy, A. K., and Gamboa-Aldeco, M. (1998). *Modern electrochemistry: an introduction to an interdisciplinary area*: Springer.
- Butler, J. (1924). Studies in heterogeneous equilibria. Part III. A kinetic theory of reversible oxidation potentials at inert electrodes. *Transactions of the Faraday Society*, 19(March), 734-739.

- Cai, X., Tanner, E. E., Lin, C., Ngamchuea, K., Foord, J. S., and Compton, R. G. (2018). The mechanism of electrochemical reduction of hydrogen peroxide on silver nanoparticles. *Physical Chemistry Chemical Physics*, 20(3), 1608-1614.
- Carriere, V. M., Rodrigues, J. P., Tan, C., Arumugam, P., and Poh, S. (2021). In vitro electrochemical detection of hydrogen peroxide in activated macrophages via a platinum microelectrode array. *Sensors*, 21(16), 5607.
- Chen, Y., Li, Q., Jiang, H., and Wang, X. (2016). Pt modified carbon fiber microelectrode for electrochemically catalytic reduction of hydrogen peroxide and its application in living cell H₂O₂ detection. *Journal of Electroanalytical Chemistry*, 781, 233-237.
- Chevallier, F. G., Davies, T. J., Klymenko, O. V., Jiang, L., Jones, T. G. J., and Compton, R. G. (2005). Numerical simulation of partially blocked electrodes under cyclic voltammetry conditions: influence of the block unit geometry on the global electrochemical properties. *Journal of Electroanalytical Chemistry*, 577(2), 211-221.
- Chuang, M.-C., Lai, H.-Y., Ho, J.-a. A., and Chen, Y.-Y. (2013). Multifunctional microelectrode array (mMEA) chip for neural-electrical and neural-chemical interfaces: characterization of comb interdigitated electrode towards dopamine detection. *Biosensors and Bioelectronics*, 41, 602-607.
- Compton, R. G., and Banks, C. E. (2011). *Understanding voltammetry*: World Scientific.
- Compton, R. G., Laborda, E., and Ward, K. R. (2013). *Understanding Voltammetry: Simulation of Electrode Processes*: Imperial College Press.
- Dantas, L., Castro, P., Peña, R., and Bertotti, M. (2014). Amperometric determination of hydrogen peroxide using a copper microelectrode. *Analytical Methods*, 6(7), 2112-2116.
- Davies, T. J., Banks, C. E., and Compton, R. G. (2005). Voltammetry at spatially heterogeneous electrodes. *Journal of Solid State Electrochemistry*, 9(12), 797-808.
- Davies, T. J., and Compton, R. G. (2005). The cyclic and linear sweep voltammetry of regular and random arrays of microdisc electrodes: Theory. *Journal of Electroanalytical Chemistry*, 585(1), 63-82.

- Davies, T. J., Moore, R. R., Banks, C. E., and Compton, R. G. (2004). The cyclic voltammetric response of electrochemically heterogeneous surfaces. *Journal of Electroanalytical Chemistry*, 574(1), 123-152.
- Dickinson, E. J. F., Limon-Petersen, J. G., Rees, N. V., and Compton, R. G. (2009). How Much Supporting Electrolyte Is Required to Make a Cyclic Voltammetry Experiment Quantitatively “Diffusional”? A Theoretical and Experimental Investigation. *The Journal of Physical Chemistry C*, 113(25), 11157-11171.
- Frebel, H., Chemnitz, G., Cammann, K., Kakerow, R., Rospert, M., and Mokwa, W. (1997). Multianalyte sensor for the simultaneous determination of glucose, L-lactate and uric acid based on a microelectrode array. *Sensors and Actuators B: Chemical*, 43(1-3), 87-93.
- Gondosiswanto, R., Hibbert, D. B., Fang, Y., and Zhao, C. (2018). Redox recycling amplification using an interdigitated microelectrode array for ionic liquid-based oxygen sensors. *Analytical Chemistry*, 90(6), 3950-3957.
- Han, J., Li, M., Li, H., Li, C., Ye, J., and Yang, B. (2020). Pt-poly (L-lactic acid) microelectrode-based microsensor for in situ glucose detection in sweat. *Biosensors and Bioelectronics*, 170, 112675.
- Haritha, V., Vijayan, A., Kumar, S. S., and Rakhi, R. (2021). Voltammetric determination of hydrogen peroxide using MoS₂ modified glassy carbon electrodes. *Materials Letters*, 301, 130258.
- Hellmann, A., Daboss, S., Zink, F., Hartmann, C., Radermacher, P., and Kranz, C. (2020). Electrocatalytically modified microelectrodes for the detection of hydrogen peroxide at blood cells from swine with induced trauma. *Electrochimica Acta*, 353, 136458.
- Huang, X. J., O'Mahony, A. M., and Compton, R. G. (2009). Microelectrode arrays for electrochemistry: approaches to fabrication. *Small*, 5(7), 776-788.
- Jia, Z., Wang, B., and Wang, Y. (2015). Copper hexacyanoferrate with a well-defined open framework as a positive electrode for aqueous zinc ion batteries. *Materials Chemistry and Physics*, 149, 601-606.
- Jiang, G., Wang, J., Yang, Y., Zhang, G., Liu, Y., Lin, H., Zhang, G., Li, Y., and Fan, X. (2016). Fluorescent turn-on sensing of bacterial lipopolysaccharide in artificial urine

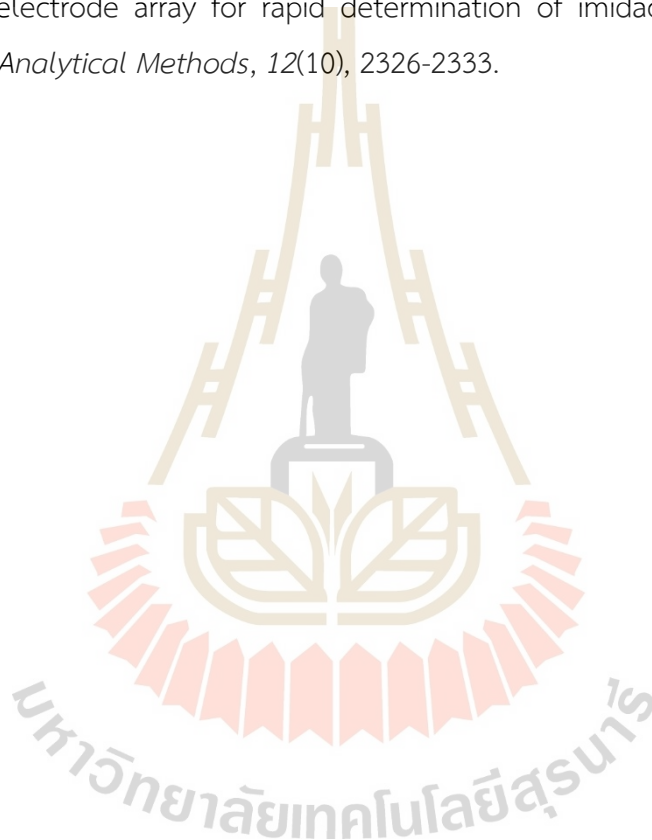
- sample with sensitivity down to nanomolar by tetraphenylethylene based aggregation induced emission molecule. *Biosens Bioelectron*, *85*, 62-67.
- Kannan, P. K., Hu, C., Morgan, H., Moshkalev, S. A., and Rout, C. S. (2016). Electrochemical sensing of bisphenol using a multilayer graphene nanobelt modified photolithography patterned platinum electrode. *Nanotechnology*, *27*(37), 375504.
- Kelly, R. S. (2009). Analytical electrochemistry: The basic concepts. *Analytical Sciences Digital Library*.
- Ledo, A., Fernandes, E., Brett, C. M., and Barbosa, R. M. (2020). Enhanced selectivity and stability of ruthenium purple-modified carbon fiber microelectrodes for detection of hydrogen peroxide in brain tissue. *Sensors and Actuators B: Chemical*, *311*, 127899.
- Lee, J.-H., Lim, T.-S., Seo, Y., Bishop, P. L., and Papautsky, I. (2007). Needle-type dissolved oxygen microelectrode array sensors for in situ measurements. *Sensors and Actuators B: Chemical*, *128*(1), 179-185.
- Li, D., Lin, C., Batchelor-McAuley, C., Chen, L., and Compton, R. G. (2019). Electrochemical measurement of the size of microband electrodes: A theoretical study. *Journal of Electroanalytical Chemistry*, *840*, 279-284.
- Li, Y., Wang, Y., Fu, C., Wu, Y., Cao, H., Shi, W., and Jung, Y. M. (2020). A simple enzyme-free SERS sensor for the rapid and sensitive detection of hydrogen peroxide in food. *Analyst*, *145*(2), 607-612.
- Liu, D., Li, M., Li, H., Li, C., Wang, G., Li, P., and Yang, B. (2021). Core-shell Au@ Cu₂O-graphene-polydopamine interdigitated microelectrode array sensor for in situ determination of salicylic acid in cucumber leaves. *Sensors and Actuators B: Chemical*, *341*, 130027.
- Liu, S., Pan, G., Li, G., and Gao, X. (2015). Copper hexacyanoferrate nanoparticles as cathode material for aqueous Al-ion batteries. *Journal of Materials Chemistry A*, *3*(3), 959-962.
- Lubello, C., Caretti, C., and Gori, R. (2002). Comparison between PAA/UV and H₂O₂/UV disinfection for wastewater reuse. *Water Science and Technology: Water Supply*, *2*(1), 205-212.

- Ma, J., and Zheng, J. (2020). Voltammetric determination of hydrogen peroxide using AuCu nanoparticles attached on polypyrrole-modified 2D metal-organic framework nanosheets. *Microchimica Acta*, 187, 1-8.
- Martins, R., Martins, D., Costa, L., Matencio, T., Paniago, R., and Montoro, L. (2020). Copper hexacyanoferrate as cathode material for hydrogen peroxide fuel cell. *International Journal of Hydrogen Energy*, 45(47), 25708-25718.
- Menshykau, D., Huang, X.-J., Rees, N. V., Del Campo, F. J., Muñoz, F. X., and Compton, R. G. (2009). Investigating the concept of diffusional independence. Potential step transients at nano-and micro-electrode arrays: theory and experiment. *Analyst*, 134(2), 343-348.
- Ng, A. M., Lim, C. T., Low, H. Y., and Loh, K. P. (2015). Highly sensitive reduced graphene oxide microelectrode array sensor. *Biosensors and Bioelectronics*, 65, 265-273.
- Ngamchuea, K., Batchelor-McAuley, C., and Compton, R. G. (2018). Anodic stripping voltammetry of silver in the absence of electrolytes: Theory and experiment. *Journal of Electroanalytical Chemistry*, 830-831, 122-130.
- Ngamchuea, K., Batchelor-McAuley, C., and Compton, R. G. (2018). Understanding electroanalytical measurements in authentic human saliva leading to the detection of salivary uric acid. *Sensors and Actuators, B*, 262, 404-410.
- Ngamchuea, K., Lin, C., Batchelor-McAuley, C., and Compton, R. G. (2017). Supported microwires for electroanalysis: sensitive amperometric detection of reduced glutathione. *Analytical Chemistry*, 89(6), 3780-3786.
- Ngamchuea, K., Lin, C., Batchelor-McAuley, C., and Compton, R. G. (2017). Supported Microwires for Electroanalysis: Sensitive Amperometric Detection of Reduced Glutathione. *Analytical Chemistry*, 89(6), 3780-3786.
- Nurbaeimah, N., Mat, N., Suryati Mohd, K., Badaluddin, N. A., Yusoff, N., Sajili, M. H., Mahmud, K., Mohd Adnan, A. F., and Khandaker, M. M. (2020). The effects of hydrogen peroxide on plant growth, mineral accumulation, as well as biological and chemical properties of *Ficus deltoidea*. *Agronomy*, 10(4), 599.
- Pravda, J. (2020). Hydrogen peroxide and disease: towards a unified system of pathogenesis and therapeutics. *Molecular Medicine*, 26(1), 1-10.

- Sanford, A. L., Morton, S. W., Whitehouse, K. L., Oara, H. M., Lugo-Morales, L. Z., Roberts, J. G., and Sombers, L. A. (2010). Voltammetric detection of hydrogen peroxide at carbon fiber microelectrodes. *Analytical Chemistry*, *82*(12), 5205-5210.
- Seddon, B., Shao, Y., and Girault, H. (1994). Printed microelectrode array and amperometric sensor for environmental monitoring. *Electrochimica Acta*, *39*(16), 2377-2386.
- Shiva, L., Ayachit, N., and Udachan, L. (2019). Electrical and microstructural properties of silver thin films. *International Journal of Nanoelectronics and Materials*, *12*, 221-236.
- Simm, A. O., Banks, C. E., Ward-Jones, S., Davies, T. J., Lawrence, N. S., Jones, T. G., Jiang, L., and Compton, R. G. (2005). Boron-doped diamond microdisc arrays: electrochemical characterisation and their use as a substrate for the production of microelectrode arrays of diverse metals (Ag, Au, Cu) via electrodeposition. *Analyst*, *130*(9), 1303-1311.
- Streeter, I., Fietkau, N., del Campo, J., Mas, R., Muñoz, F. X., and Compton, R. G. (2007). Voltammetry at regular microband electrode arrays: Theory and experiment. *The Journal of Physical Chemistry C*, *111*(32), 12058-12066.
- Suliman, M., Addy, M., MacDonald, E., and Rees, J. (2004). The effect of hydrogen peroxide concentration on the outcome of tooth whitening: an in vitro study. *Journal of Dentistry*, *32*(4), 295-299.
- Tan, F., Metters, J. P., and Banks, C. E. (2013). Electroanalytical applications of screen printed microelectrode arrays. *Sensors and Actuators B: Chemical*, *181*, 454-462.
- Toh, H. S., Batchelor-McAuley, C., Tschulik, K., Uhlemann, M., Crossley, A., and Compton, R. G. (2013). The anodic stripping voltammetry of nanoparticles: electrochemical evidence for the surface agglomeration of silver nanoparticles. *Nanoscale*, *5*(11), 4884-4893.
- Uchida, M., and Ono, M. (1999). Determination of hydrogen peroxide in beer and its role in beer oxidation. *Journal of the American Society of Brewing Chemists*, *57*(4), 145-150.

- Ugarte, A., Gil-Bea, F., García-Barroso, C., Cedazo-Minguez, Á., Ramírez, M. J., Franco, R., García-Osta, A., Oyarzabal, J., and Cuadrado-Tejedor, M. (2015). Decreased levels of guanosine 3', 5'-monophosphate (c GMP) in cerebrospinal fluid (CSF) are associated with cognitive decline and amyloid pathology in Alzheimer's disease. *Neuropathology and Applied Neurobiology*, 41(4), 471-482.
- Wang, J., Wang, Y., Cui, M., Xu, S., and Luo, X. (2017). Enzymeless voltammetric hydrogen peroxide sensor based on the use of PEDOT doped with Prussian Blue nanoparticles. *Microchimica Acta*, 184, 483-489.
- Wang, X., Sun, L., Wang, T., and Shi, Y. (2020). Temperature-compensated pH microelectrode array sensors based on copper-oxide/polyaniline modification. *IEEE Sensors Journal*, 20(24), 14598-14606.
- Ward Jones, S. E., Campbell, F. W., Baron, R., Xiao, L., and Compton, R. G. (2008). Particle Size and Surface Coverage Effects in the Stripping Voltammetry of Silver Nanoparticles: Theory and Experiment. *The Journal of Physical Chemistry C*, 112(46), 17820-17827.
- Watkins, S. (2009). Comparison of hydrogen peroxide products for water sanitation. *The Poultry Site*.
- Wei, A. C. Chemistry of electronic materials.
- Wessells, C. D., Huggins, R. A., and Cui, Y. (2011). Copper hexacyanoferrate battery electrodes with long cycle life and high power. *Nature Communications*, 2(1), 1-5.
- Winterbourn, C. C. (2013). The biological chemistry of hydrogen peroxide. *Methods in Enzymology*, 528, 3-25.
- Yamada, Y., Yoneda, M., and Fukuzumi, S. (2013). A Robust One-Compartment Fuel Cell with a Polynuclear Cyanide Complex as a Cathode for Utilizing H₂O₂ as a Sustainable Fuel at Ambient Conditions. *Chemistry—A European Journal*, 19(35), 11733-11741.
- Yang, H., Rahman, M. T., Du, D., Panat, R., and Lin, Y. (2016). 3-D printed adjustable microelectrode arrays for electrochemical sensing and biosensing. *Sensors and Actuators B: Chemical*, 230, 600-606.

- Yilbas, B. S., Al-Sharafi, A., and Ali, H. (2019). Chapter 3 - Surfaces for Self-Cleaning. In B. S. Yilbas, A. Al-Sharafi, and H. Ali (Eds.), *Self-Cleaning of Surfaces and Water Droplet Mobility* (pp. 45-98): Elsevier.
- Zhang, J., Zhao, M., Yang, J., Wu, G., Wu, H., Chen, C., and Liu, A. (2019). Metal-free rGO/GO hybrid microelectrode array for sensitive and in-situ hydrogen peroxide sensing. *Electrochimica Acta*, 326, 134967.
- Zhang, W., Liu, C., Zou, X., Zhang, H., and Xu, Y. (2019). A β -CD/MWCNT-modified-microelectrode array for rapid determination of imidacloprid in vegetables. *Food Analytical Methods*, 12(10), 2326-2333.



CURRICULUM VITAE

Name: Keerakit Kaewket

Phone number: (+66)641928655

Address: 262 Village No.10 Joho Sub-district, Muang Nakhon Ratchasima District,
Nakhon Ratchasima, 30310, Thailand

E-mail: kaewketkeerakit41@gmail.com

Education Background

- 2021- present: Master of Science (Chemistry), Suranaree University of Technology
- 2017 – 2021: Bachelor of Science (Chemistry, First class honor), Suranaree University of Technology

Publications

- ‘Adsorptive stripping voltammetry at microporous carbon: Determination and adsorption characteristics of environmental contaminants.’ **Kaewket K**, Maeansiri S, Ngamchuea K, *Colloid and Interface Science Communications*, 2020, 38, 100310.
- ‘Anti-fouling Effects of Carbon Nanofiber in Electrochemical Sensing of Phenolic Compounds.’ **Kaewket K**, Karuwan C, Sonsupap S, Maeansiri S, Ngamchuea K, *Journal of The Electrochemical Society*, 2021, 168 (6), 067501.
- ‘Silver Microelectrode Arrays for Direct Analysis of Hydrogen Peroxide in Low Ionic Strength Samples.’ **Kaewket K**, Janphuang P, Laohana P, Tanapongpisit N, Saenrang W, Ngamchuea K, *Electroanalysis*, 2022, 1040-0397.
- ‘Microporous carbon for fast and simple electrochemical detection of imidacloprid insecticide in fruit and water samples.’ **Kaewket K**, Ngamchuea K, *RSC Advances*, 2023, 13(7), 4532-4541.

Award

- Metrohm-CST Young Chemist Award from the Chemical Society of Thailand